Cell-extrinsic mechanical forces restore neutrophil polarization in the absence of branched actin assembly

Brian R. Graziano[1], Jason P. Town[1], Tamas L. Nagy[1], Miha Fošnarič[4], Samo Penič[3], Aleš Iglič[3,6], Veronika Kralj-Iglič[4,6], Nir Gov[5], Alba Diz-Muñoz[2], and Orion D. Weiner[1*]

1. Cardiovascular Research Institute and Department of Biochemistry and Biophysics, University of California, San Francisco
2. Cell Biology and Biophysics Unit, European Molecular Biology Laboratory, Heidelberg, Germany
3. Department of Theoretical Electrotechnics, Mathematics and Physics, Faculty of Electrical Engineering, University of Ljubljana, Slovenia
4. Faculty of Health Sciences, University of Ljubljana, Slovenia
5. Department of Chemical and Biological Physics, Weizmann Institute, Rehovot, Israel
6. Laboratory of Clinical Biophysics, Faculty of Medicine, University of Ljubljana, Slovenia

* To whom correspondence should be addressed:
Orion Weiner
CVRI & Department of Biochemistry and Biophysics
University of California, San Francisco
Cardiovascular Research Building, Room 352F, MC 3120
555 Mission Bay Blvd. South
San Francisco, CA 94158
Tel. 415-514-4352, Fax 415-514-1176
Email: orion.weiner@ucsf.edu

ABSTRACT

For directed movement, cells must constrain protrusions to a limited region of their surface. Both the local positive and global negative feedback loops that generate polarity are thought to be regulated by actin polymerization. However, the types of actin networks contributing to feedback and the underlying mechanisms remain unclear. Here we show that branched actin networks assembled by Arp2/3 and WAVE complex are essential for proper neutrophil polarity and motility in unconfined environments. In contrast, confined cells use a distinct mode of leading-edge advance and polarization whose regulatory positive and negative feedback loops do not depend on branched actin networks. By applying physical perturbations to the plasma membrane, we find that the long-range inhibitor enabling front competition does not solely respond to changes in membrane tension. This work revises our understanding of the core neutrophil polarity network and indicates that cells have distinct molecular circuits for polarity that dominate in different environments.

INTRODUCTION

Directed migration underlies a wide array of biological processes, including embryogenesis, wound healing, and the ability of immune cells to track and destroy pathogens. A key step in migration is polarization, where cells restrict the activity of their protrusive machinery to a limited portion of their surface. Polarization is thought to arise through the coordinated interactions of short-range positive and long-range negative feedback loops, with actin polymerization playing essential roles in both types of feedback (Devreotes et al., 2017; Krause and Gautreau, 2014; Saha et al., 2018).

When migratory cells first sense a spatially uniform increase in stimulatory cues, they respond by rapidly activating leading-edge polarity factors, including RhoGTPases (e.g., Rac), throughout the plasma membrane (Weiner et al., 2007; Yang et al., 2016). These GTPases, in turn, activate Arp2/3-driven assembly of branched actin networks by recruiting nucleation-promoting factors (NPFs) such as WAVE and WASP (Fritz-Laylin et al., 2017; Machesky and Insall, 1998; Veltman et al., 2012; Weiner et al., 2006). Each of these nascent polarity sites is sustained by multiple short-range positive feedback loops (e.g., recruitment of additional RhoGTPase activators (Nguyen et al., 2016)), in a manner that often depends on actin assembly (Inoue and Meyer, 2008; Srinivasan et al., 2003; Weiner et al., 2002). In parallel with this initial step of activation—but occurring on a slower timescale—cells generate long-range negative feedback to enable a dominant front to emerge (Swaney et al., 2010). In neutrophils, cells of the innate immune system, this process occurs through the growth of actin filaments, which stretch and increase tension in the plasma membrane (Houk et al., 2012). This membrane tension acts as a long-range inhibitor of actin nucleation and polymerization, which enables a “winner-takes-all” competition among the nascent polarity sites to produce a single protrusion (**Fig. 1A**) (Diz-Muñoz et al., 2016; Houk et al., 2012; Keren et al., 2008; Sens and Plastino, 2015).

While actin polymerization serves as a key ingredient in generating the positive and negative feedback loops that give rise to polarity, we lack an understanding of how specific types of actin networks provide each kind of feedback. Immune cells assemble multiple actin networks at different subcellular locations that carry out distinct functions to support migration: Arp2/3-dependent assembly of branched actin networks at the leading edge contributes to cell guidance/steering and protrusion extension, while actomyosin bundles near the trailing edge provide contractile force to lift the cell rear and squeeze the cell body forward (Lämmermann and Germain, 2014; Moreau et al., 2018). Along with these functional differences, the types of actin networks immune cells and other migratory cells employ for migration vary with microenvironment (Lämmermann and Germain, 2014; Paluch et al., 2016). The role of actin dynamics in migration is thus highly nuanced and depends on the type of actin network, its subcellular location, as well as the extracellular environment. In contrast, the data implicating actin polymerization in both the positive and negative feedback loops needed for polarity are largely based on pharmacological perturbations that target all actin polymer (Diz-Muñoz et al., 2016; Huang et al., 2013; Inoue and Meyer, 2008; Sasaki et al., 2007; Wang et al., 2002; Weiner et al., 2007; Yang et al., 2016). This discrepancy raises the question of how different subcellular actin networks contribute to polarity generation under different environmental conditions.

Here, we address this question by dissecting the role of branched actin assembly in the neutrophil polarity program. We use CRISPR-mediated genome editing to knock out either the Arp2/3 complex (the nucleator of branched actin assembly (Mullins et al., 1998; Welch et al., 1997)) or its key activator the WAVE complex (Machesky et al., 1999) in human neutrophils (differentiated HL-60 cells). We find that during unconfined migration, WAVE-dependent actin assembly is required for the mechanical force generation that supports long-range negative feedback. However, the WAVE complex is dispensable for polarity and movement of confined cells, where cell-*extrinsic* mechanical forces can compensate for the cell-*intrinsic* forces normally produced by WAVE complex. This confined movement relies on a completely different mode of leading-edge advance, with processive bleb-like protrusions forming in a back-and-forth motion that extends the leading edge in a serpentine manner. Surprisingly, these serpentine protrusions coincide with Rac-based local positive feedback loops that operate independently of branched actin assembly, suggesting a separate polarity circuit in this context. Finally, we find that the long-range inhibitor that underlies competition between protrusions does not always respond to membrane tension directly but may rely on closely linked properties such as cell shape, and local membrane curvature. Our data challenge longstanding assumptions regarding the roles of branched actin assembly in generating cell polarity and movement. Rather than being a key player under all conditions migratory cells may experience, the importance of branched actin assembly in consolidating polarity process varies greatly with microenvironment.

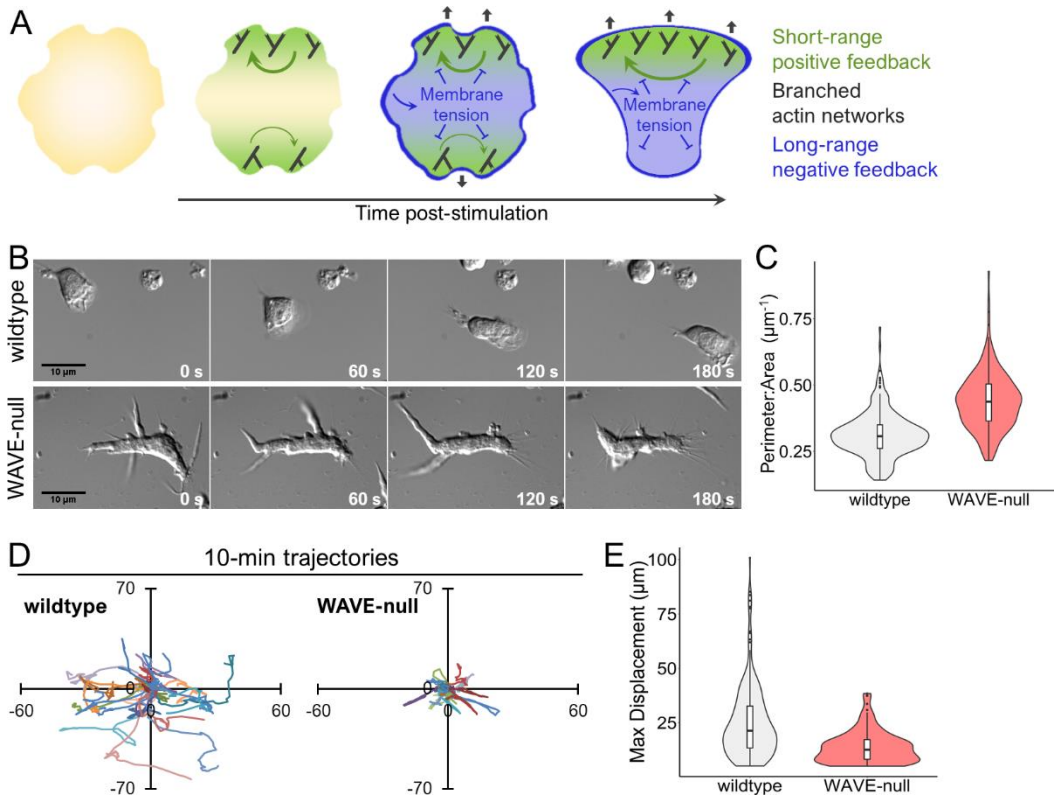

Figure 1. WAVE complex is required for neutrophil polarity and motility.

A) Polarity generation depends on fast-acting, short-range positive feedback and slower-acting, long-range negative feedback. Actin assembly participates in both types of feedback, with its role in negative feedback arising from mechanical force production at the plasma membrane.

B) Migration of differentiated HL-60 cells (dHL-60s) on fibronectin-coated glass in uniform chemoattractant (10 nM fMLP) visualized with differential interference contrast (DIC) microscopy.

C) Perimeter-to-area ratios of cells were calculated as described in "Materials and methods". N = 211 wildtype and 198 WAVE-null cells pooled from 2 independent experiments.

D-E) dHL-60s were prepared as in B. Cells were tracked using NucBlue nuclear stain and imaged every 15 s by widefield epifluorescence microscopy. **D)** Representative tracks from 30 wildtype and 30 WAVE-null cells (randomly selected) over a 10-min observation window. Axes, distance in μm. **E)** Maximum displacement measurements. Each point in the distribution represents the furthest a cell moved relative to its initial starting position over the 10-min observation period. N = 338 wildtype and 278 WAVE-null cells pooled from 2 independent experiments.

RESULTS

WAVE complex is required for polarization during adhesion-dependent migration

The WAVE complex is required for proper leading edge formation in immune cells (Leithner et al., 2016; Weiner et al., 2006) and its role in regulating cell shape and motility is broadly conserved across metazoans (Blagg et al., 2003; Kunda et al., 2003; Shakir et al., 2008). To generate a human neutrophil cell line lacking the WAVE complex (hereafter referred to as 'WAVE-null'), we used

CRISPR-Cas9 to knock out *HEM1/NCKAPL1*, which encodes the sole hematopoietic-specific component of the pentameric WAVE complex (Weiner et al., 2006), in dHL-60 cells. Disruption of *HEM1* is preferable to targeting *WAVE2/WASF2* directly since loss of HEM1 results in the concomitant degradation of the other remaining subunits of WAVE complex, including WAVE2 (**Fig. S1A**), and avoids potentially confounding gain-of-function effects of partial sub-complexes (Leithner et al., 2016; Litschko et al., 2017; Weiner et al., 2006).

As expected, WAVE-null cells showed severe polarity and morphological defects when plated in a standard 2-D adhesion setting. Treatment of WAVE-null cells with uniform chemoattractant resulted in the production of multiple dynamic finger-like protrusions radiating from the cell surface in a non-polarized fashion, rather than a single smooth leading edge typically observed in wildtype cells (**Fig. 1B and Videos 1-2**). To quantify cell morphology, we calculated the perimeter-to-area ratio of cells, where compact cells with smooth edges would be expected to have smaller values than cells with an extended 'dendritic' morphology. Consistent with this idea, the mean ratios for wildtype and WAVE-null cells were 0.31 ± 0.01 μm^{-1} and 0.44 ± 0.01 μm^{-1}, respectively (**Fig. 1C**). WAVE-null cells also showed pronounced motility defect during chemokinesis: When observed over a 10-min period, WAVE-null cells showed a mean maximum displacement of 14 ± 1 μm from their initial positions vs. 25 ± 1 μm for wildtype cells (**Fig. 1D-E**). The phenotypes we observed are broadly similar to those reported in mouse dendritic cells lacking WAVE complex (Leithner et al., 2016), in that both cell types failed to form lamellipod-like protrusions at the leading edge. However, 'WAVE-null' mouse dendritic cells showed only mildly impaired motility and appeared to have only a minor polarity defect. These differences may arise from the distinct physiological functions these two cell types perform (Lämmermann and Germain, 2014). We also note that the polarity defects we observed in WAVE-null neutrophils were more severe than those reported in prior work using RNAi to knockdown the HEM1 subunit of WAVE complex (Weiner et al., 2006). As our CRISPR-based approach eliminates all protein, the milder defects observed upon HEM1 knockdown may arise from the residual amounts of WAVE complex following RNAi.

The multipolar phenotype we observed in WAVE-null neutrophils could arise from a defect in membrane tension generation (**Fig. 2A**), which is needed for producing the negative feedback that fronts use to compete with one another (Houk et al., 2012; Raucher and Sheetz, 2000). To test this idea, we used atomic force microscopy (AFM) to measure membrane tether force in cells stimulated with chemoattractant (**Fig. 2B**). WAVE-null cells showed a two-fold decrease in tether force vs. wildtype cells (**Fig. 2B**), corresponding to a four-fold decrease in membrane tension (see (Dai and Sheetz, 1995) for calculation details). These results could arise if WAVE-null cells are defective in the actin polymerization that provides the mechanical force that generates membrane tension (Diz-Muñoz et al., 2016; Houk et al., 2012) (**Fig. 1A**, blue lines; **Fig. 2A**). To test this idea, we stimulated neutrophils with a uniform increase in chemoattractant and observed cellular levels and distribution of filamentous actin (F-actin). Following stimulation, F-actin levels in wildtype cells initially doubled as neutrophils drove actin assembly uniformly across the plasma membrane. F-actin levels later decreased, coinciding with the formation of a single actin-rich protrusion (**Fig. 2C-D**). This behavior is consistent with prior work (Diz-Muñoz et al., 2016) and broadly reflects the coordinated positive and negative feedback loops giving rise to polarity (**Fig. 1A**). WAVE-null

cells, in contrast, exhibited only modest increases in F-actin initially (60 s) following stimulation (67 ± 7% increase for WAVE-null cells vs. 150 ± 30% increase for wildtype cells). However, WAVE-null cells maintained these F-actin increases for at least 600 s (**Fig. 2D**), consistent with these cells failing to spatially restrict protrusion growth to a single location (**Fig. 2C**). Mis-regulation of F-actin levels in WAVE-null cells is dominated by differences in actin assembly since turnover rates and total actin levels are similar in both wildtype and WAVE-null cells (**Fig. S2A-B**). The increased F-actin levels in WAVE-null cells 5-10 min post-stimulation ran counter to our expectations: Our previous work using a variety of genetic and drug-based perturbations revealed a strong linear correlation between cellular F-actin levels and membrane tension in cells stimulated with chemoattractant for 5-10 min (Diz-Muñoz et al., 2016). Neutrophils lacking WAVE complex do not follow this relation. Despite WAVE-null cells maintaining ~1.5-fold higher F-actin levels than wildtype cells, their membrane tension is similar to that of wildtype cells treated with actin assembly-blocking drugs (**Fig. 2E**). Our results show that WAVE-dependent actin assembly is required for efficient generation of membrane tension increases and indicate that not all types of actin polymer are equivalent for membrane tension generation.

We further performed computational simulations to assess whether changes in the spatial organization of actin nucleation correlated with changes in membrane tension. By modulating the curvature preference of a fixed concentration of actin nucleators, we generated membrane surfaces ranging from those containing multiple finger-like protrusions (similar to WAVE-null cells) to a single sheet-like protrusion (similar to wildtype cells). Transition in membrane shape from finger-like to sheet-like coincided with increases in membrane tension (**Fig. 2F and S3**). These simulations show that even if the concentration of actin nucleators remains constant, changes in their organization can affect the amount of membrane tension they can generate as well as the morphology of the resulting protrusions they form. In combination with our experimental data, they suggest that spatial organization of WAVE complex at the plasma membrane is a major factor contributing to WAVE complex's ability to generate lamellipod-like protrusions and that protrusions with this morphology may be more effective at increasing membrane tension than other protrusion types.

Furthermore, the simulations indicate that the spontaneous curvature of the actin nucleators has profound effects on the overall morphology of the simulated vesicles. Flat, lamellipodia-like shapes are obtained for highly curved nucleators, while multiple finger-like protrusions are found for actin nucleators that are flat (**Fig. 2F**). Comparing these phenotypes to the observed wildtype and WAVE-null cells (**Fig. 1B**) suggests that the WAVE is associated with a high spontaneous curvature, while the nucleators that drive the actin polymerization in the finger-like protrusions of the WAVE-null cells have a very low preferred curvature.

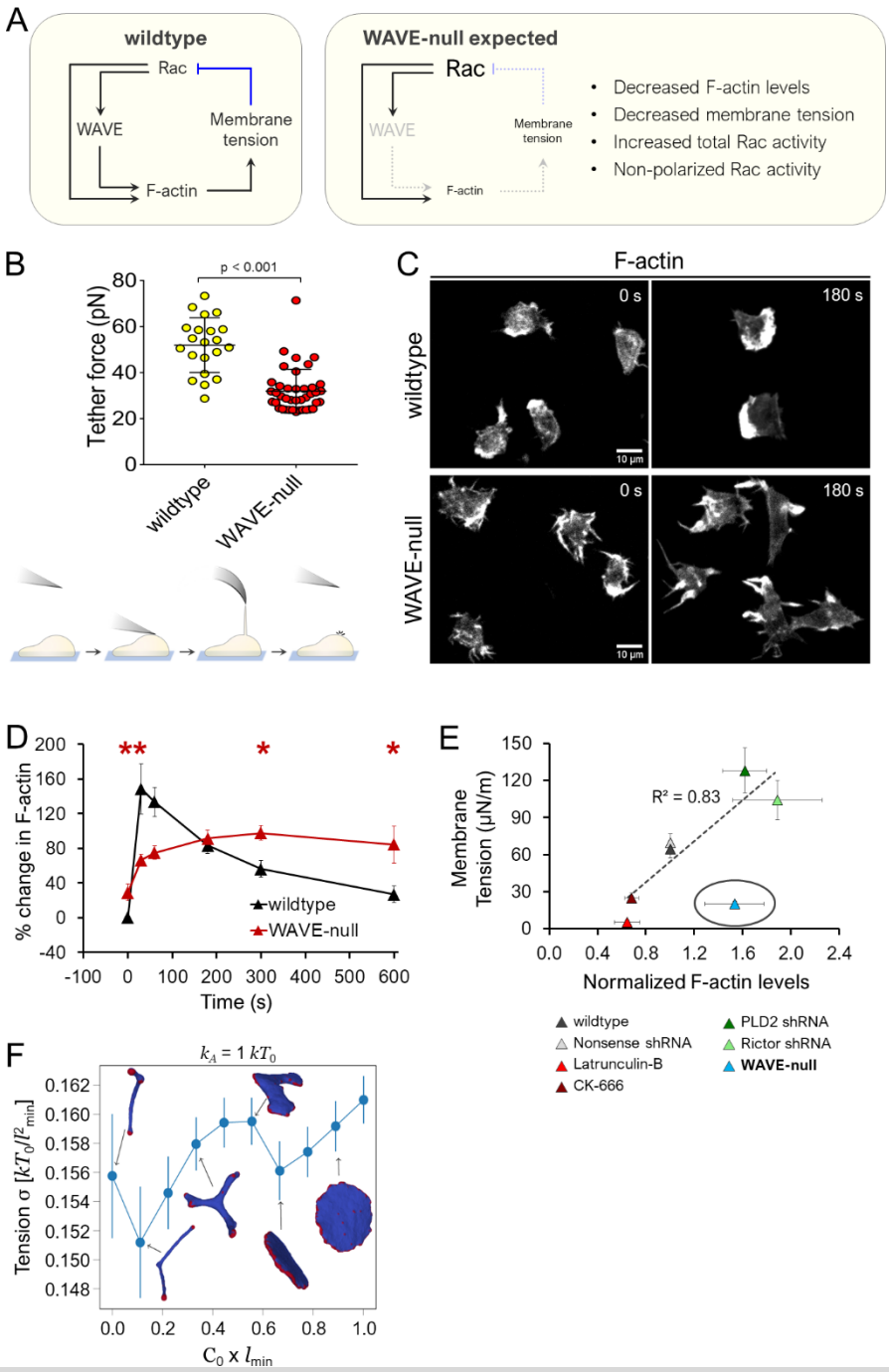

Figure 2. WAVE-null cells have decreased membrane tension despite elevated actin assembly.

A) Left, schematic depicting key components in the neutrophil polarity circuit. Right, expected regulatory changes in the absence of WAVE complex.

B) Top, Membrane tether force was measured using atomic force microscopy (AFM) in dHL-60s cells plated for at least 10 min in 10 nM fMLP. Each point represents a single cell. Data were pooled from 3 independent experiments. Error bars, SD. Bottom, Schematic depicting the experimental procedure. An AFM cantilever was briefly brought into contact with a cell, then withdrawn. In instances when a membrane tether was successfully pulled, the cantilever was maintained at a constant height until the tether broke. The change in cantilever deflection was used to measure the 'tether force'.

C) dHL-60s in suspension were fixed and stained for F-actin using rhodamine-phalloidin in the presence or absence of chemoattractant (100 nM fMLP).

D) F-actin levels for cells stimulated with 100 nM fMLP and fixed in suspension were determined by flow cytometry. Each point is an average of 7 independent experiments where the mean fluorescence of >10,000 cells was measured. Error bars, SEM. *, $P < 0.05$ by unpaired t-test.

E) Plasma membrane tension as a function of cellular F-actin levels. Each triangle represents an average of at least 11 cells for each indicated RNAi or drug-based perturbation. Dashed grey line, best-fit (least squares method) excluding WAVE-null cells within the grey circle. Error bars, SEM. All data except for those obtained from WAVE-null cells are reproduced from our prior work (see Fig. S5C in Diz-Muñoz et al., 2016) to aid in comparison.

F) Membrane tension σ (see "Materials and Methods") as a function of spontaneous curvature, c_0, of actin nucleators. Averaging was performed over 200 statistically independent microstates in equilibrium. Actin nucleators, red. Protein-free lipid bilayer, blue. Error bars, SD.

Key leading-edge polarity factors require WAVE complex for proper regulation

Membrane tension plays a major role in negatively regulating the polarity factors that organize protrusion growth, including the RhoGTPase Rac (Houk et al., 2012; Lieber et al., 2013). The morphological polarity defects observed in WAVE null cells are expected based on the decreased membrane tension in these cells, which should fail to engage the global negative feedback circuit that constrains the amounts and spatial distribution of Rac activity. We tested this hypothesis by monitoring the levels of Rac activation using the phosphorylation state of Pak kinase, a Rac effector (Knaus and Bokoch, 1998). Following stimulation, WAVE-null cells produced significantly higher levels phospho-Pak than wildtype cells (**Fig. 3A**), consistent with elevated levels of Rac activity. This result is also in agreement with recent work revealing a role for actin polymerization in negatively regulating Rac activity in neutrophils (Graziano et al., 2017).

We next examined whether elevated levels of Rac activity coincided with failure to restrict Rac activity to a single site. Using the PakPBD biosensor (Manser et al., 1994; Weiner et al., 2007), we monitored the spatial distribution of Rac activity in live cells. Stimulation of wildtype cells with uniform chemoattractant produced an initial burst of Rac activity throughout the plasma membrane, followed by its restriction to a single protrusion (**Fig. 3B**, top row; **Video 3**), in agreement with prior work (Weiner et al., 2007; Yang et al., 2016). WAVE-null cells, in contrast, maintained multiple protrusions enriched for Rac activity for the entire timecourse (**Fig. 3B**, bottom row; **Video 4**). We quantified polarity in these cells by measuring the distance between the geometric cell center and the center of weighted Rac activity signal, followed by normalization using the cell length (**Fig. 3D**). This yields a 'Rac polarity' score from 0 to 1, with a value of '0' indicating Rac activity distributed uniformly around the cell and a value near '1' indicating a single focus of Rac activity on the portion of the membrane furthest from the cell center (see Methods for details). Populations of wildtype neutrophils polarized Rac activity in response to uniform chemoattractant, with cells reaching peak polarity around 60 s (**Fig. 3C**). In contrast, WAVE-null cells showed no Rac polarity increase following stimulation with chemoattractant (**Fig. 3C**), consistent with impaired spatial regulation of Rac activity (**Fig. 3E**).

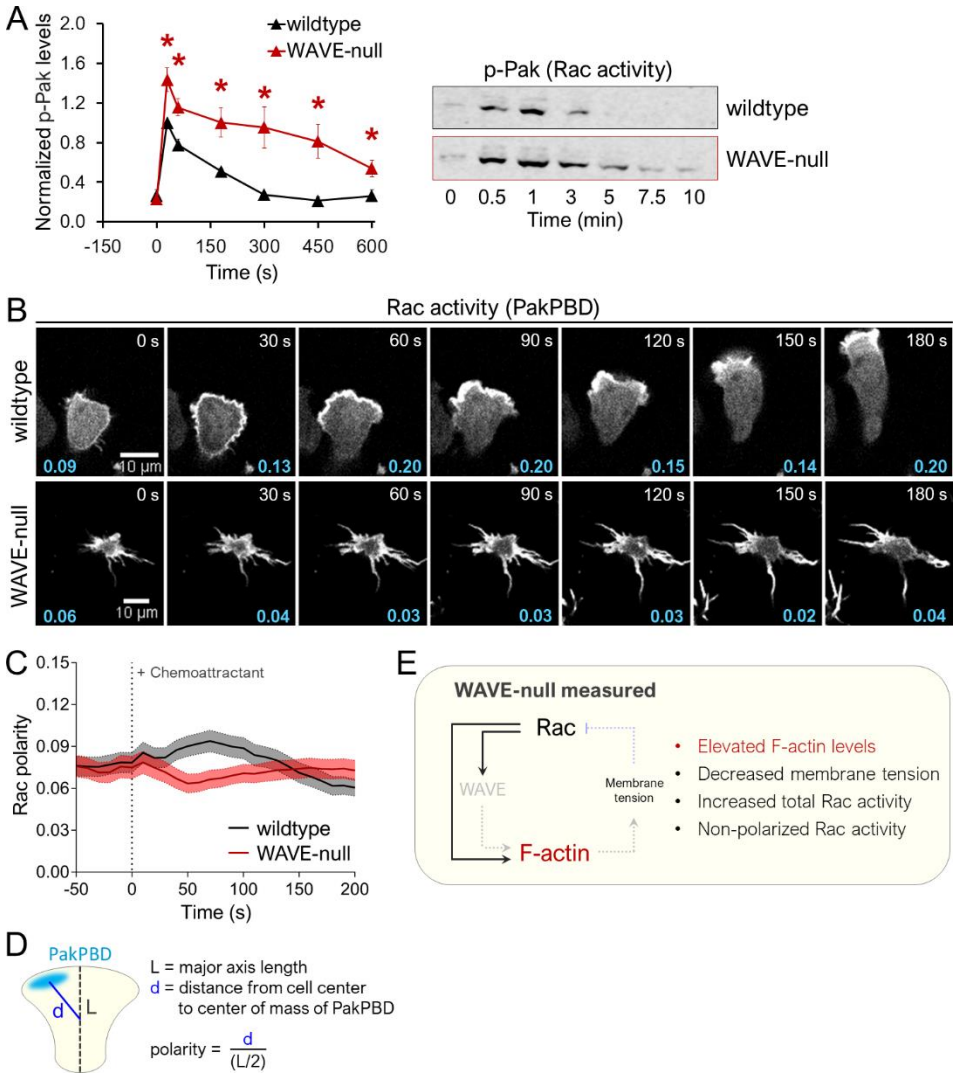

Figure 3. Loss of WAVE complex results in aberrant Rac activity.

A) Rac activity was quantified for chemoattractant-stimulated cells using antibodies targeting phospho-Pak, a downstream readout of Rac activation. Antibodies targeting total Pak were used as loading controls. Left, each point represents an average of 4 independent experiments, with data for each experiment normalized to wildtype cells at '0 s'. Error bars, SEM. *, $P < 0.05$ by unpaired t-test. Right, representative immunoblot.

B) dHL-60 cells expressing the Rac biosensor PakPBD-mCitrine were plated on fibronectin-coated glass, stimulated with 100 nM fMLP, and imaged by confocal microscopy every 10 s. Values in cyan indicate the degree of PakPBD polarization, as described in D.

C) dHL-60s were prepared as in B, and polarity of Rac activity was measured for single cells at each 10-s interval. Dark lines, mean polarity of Rac activity. Light shaded regions, +/- 95% CI of the mean. N = 211 wildtype and 198 WAVE-null cells pooled from 2 independent experiments.

D) Schematic depicting calculation of Rac activity polarity. See "Materials and Methods" for details.

E) Schematic depicting measured regulatory changes among key polarity components in the absence of WAVE complex. Compare with expected changes in 2A.

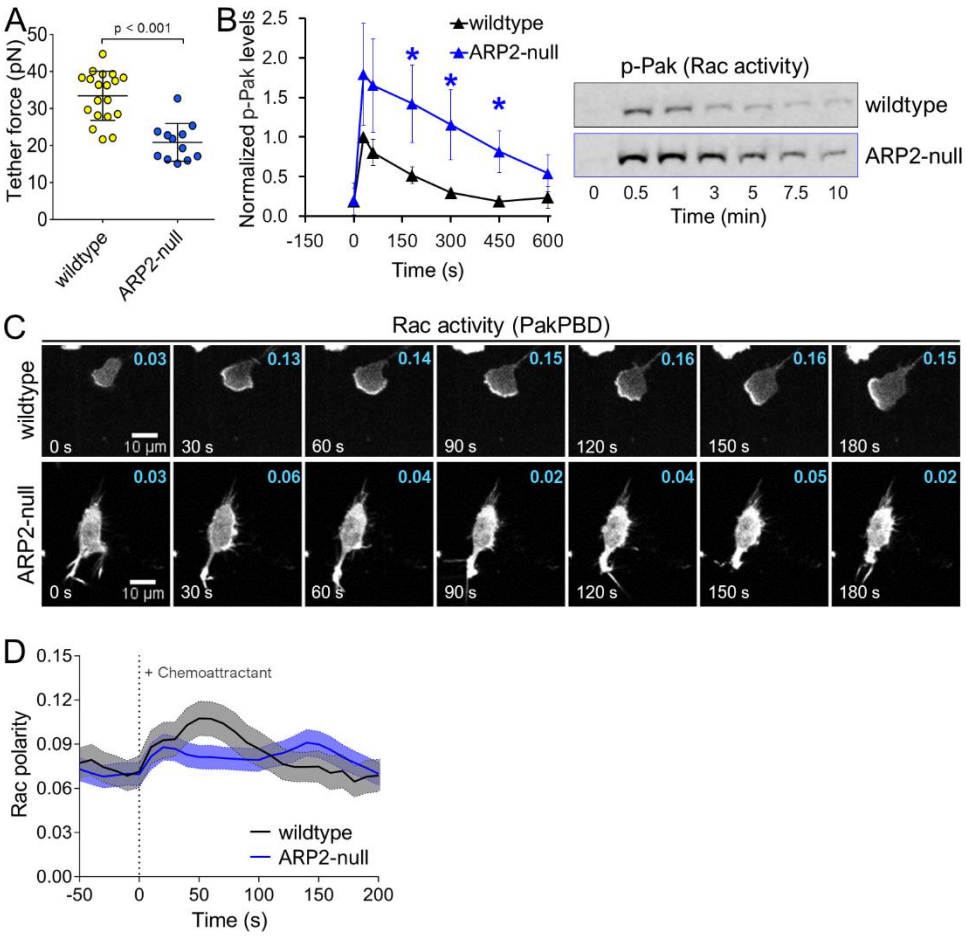

Figure 4. Loss of Arp2/3 complex phenocopies polarity defects observed in WAVE-null cells.

A) Membrane tether force of dHL-60s was measured using AFM as described in 2B. Each point represents a single cell. Data were pooled from 2 independent experiments. Error bars, SD.

B) dHL-60s were stimulated with 10 nM fMLP and samples were collected and processed for immunoblot. Left, Rac activity was indirectly quantified as in 3A. Each point represents an average of 4 independent experiments, with data for each experiment normalized to wildtype cells at '0 s'. Error bars, SEM. *, P < 0.05 by unpaired t-test. Right, representative immunoblot.

C) dHL-60 cells expressing PakPBD-mCitrine were imaged as in 3B. Values in cyan indicate the degree of PakPBD polarization, as described in 3D.

D) Quantification of Rac polarity as described in 3D for cells prepared as in C. Dark lines, mean Rac polarity. Light shaded regions, +/- 95% CI of the mean. N = 101 wildtype and 185 ARP2-null cells pooled from 2 independent experiments.

A major cellular function of the WAVE complex is stimulation of Arp2/3-dependent branched actin assembly, but the WAVE complex's ability to regulate Rac could also stem from its additional roles. In other systems, the WAVE complex interacts with regulators of Rac (e.g., Rac GAPs (Soderling et al., 2002)) or additional actin assembly factors (e.g., formins (Beli et al., 2008)). Furthermore, the WAVE complex may contribute to the growth of actin networks nucleated by WAVE-

independent processes (Bieling et al., 2018). To test whether such Arp2/3-*independent* functions of the WAVE complex may contribute to its role in Rac regulation, we performed additional experiments in cells lacking functional Arp2/3 complex (**Fig. S1B**). These 'ARP2-null' cells phenocopied the key defects we observed in WAVE-null neutrophils: ARP2-null cells showed impaired membrane tension generation (**Fig. 4A**), elevated levels of Rac activity (**Fig. 4B)**, and diminished polarization of Rac activity in response to stimulation with uniform chemoattractant (**Fig. 4C-D**). These data demonstrate that WAVE complex primarily regulates polarity through its stimulation of branched actin assembly rather than through its other cellular functions.

Hypotonic treatment restores polarity in the absence of WAVE complex

If the WAVE complex primarily regulates long-range inhibition of leading-edge signals by imparting mechanical force on the plasma membrane, we should be able to restore long-range inhibition by providing compensatory mechanical forces. One approach for mimicking WAVE's extension of the plasma membrane is to place neutrophils in hypotonic media, where osmotic-based cell swelling may provide such a force (**Fig. 5A**) (Gauthier et al., 2011; Houk et al., 2012). Since wildtype neutrophils can still polarize and migrate in 0.5x isotonic media (i.e. a 1:1 dilution of isotonic media with deionized water) (Diz-Muñoz et al., 2016), we examined how stimulating WAVE-null cells under similar conditions affected the amount of Rac activity. In 0.5x isotonic media, both wildtype and WAVE-null cells showed nearly identical levels of Rac activity throughout the entire timecourse (as assayed via Pak phosphorylation, **Fig. 5B**), indicating a rescue of the Rac activity defect observed in WAVE null cells in isotonic media (**Fig. 3A**). These data suggest that hypotonic treatment can supply the mechanical force that is normally provided by WAVE-dependent actin assembly to generate the negative feedback needed for limiting total cellular Rac activity.

We next examined what physical changes the WAVE complex might impart on the plasma membrane to regulate Rac activity. Prior work concluded that membrane tension increases play a primary role in this regulatory behavior: Experimental perturbations that increase membrane tension lead to inhibition of both Rac and the WAVE complex; conversely, decreases in membrane tension lead to their activation throughout the cell (Houk et al., 2012). However, tension increases frequently coincide with other physical changes (e.g., unfolding of membrane reservoirs (Hallett et al., 2008; Sens and Plastino, 2015)), and it is not clear whether membrane tension itself or a close correlate forms the basis of the long-range inhibition. Determining whether membrane tension or other physical parameters execute the long-range inhibition is critical to identifying the relevant mechanosensor that orchestrates this process (Diz-Muñoz et al., 2013). Using AFM to measure membrane tether force, we were surprised to find that mild hypotonic treatment of WAVE-null cells did not increase membrane tension (**Fig. 5C**), so the rescue of Rac activity by hypotonic treatment is not a consequence of increased membrane tension. However, hypotonic shock did cause other alterations to the organization of the membrane of WAVE-null cells that normally go along with tension changes. In particular, volume increased by as much as two-fold (**Fig. 5D**), indicating a significant increase in the apparent surface area of the membrane (Hallett

et al., 2008). These observations are consistent with leukocytes maintaining membrane reservoirs that can be released in response to osmolarity decreases (Cheung et al., 1982; Ting-Beall et al., 1993). Furthermore, they indicate that polarity-regulating mechanosensors respond to physical changes in the plasma membrane beyond tension increases.

Along with the role of actin polymerization in generating long-range inhibition, there is also a well-established requirement for actin assembly in mediating short-range positive feedback during polarization of migratory cells (Huang et al., 2013; Inoue and Meyer, 2008; Nguyen et al., 2016; Sasaki et al., 2007; Wang et al., 2002; Weiner et al., 2007; Yang et al., 2016 ; **Fig. 1A**, green arrows). However, the conclusions from much of this earlier work were based on experiments where all actin networks were disrupted via drug treatment, leaving open the question of which actin networks might provide short-range positive feedback to Rac activity. Using our WAVE-null neutrophils, we revisited this question by testing the role of WAVE-dependent actin assembly in providing short-range positive feedback. We investigated whether hypotonic treatment (i.e. restoration of long-range negative feedback) might also restore short-range positive feedback by quantifying polarization of Rac activity using PakPBD localization. WAVE-null cells in 0.5x isotonic media could mildly polarize Rac activity in response to chemoattractant (**Fig. 5E-F; Videos 5-6**), whereas they had failed to do so in 1.0x isotonic media (**Fig. 3B-C**). However, hypotonic treatment did not affect protrusion morphology, which remained finger-like (**Fig. 5E**, bottom row). This partial rescue of polarity is surprising since branched actin assembly at the leading edge has been generally assumed to be required for short-range positive feedback. Contrary to these expectations, our results show that other mechanisms may function independent of the WAVE complex to produce short-range positive feedback, so long as the requirement for long-range negative feedback (i.e. mechanical force) is satisfied (**Fig. 5G**).

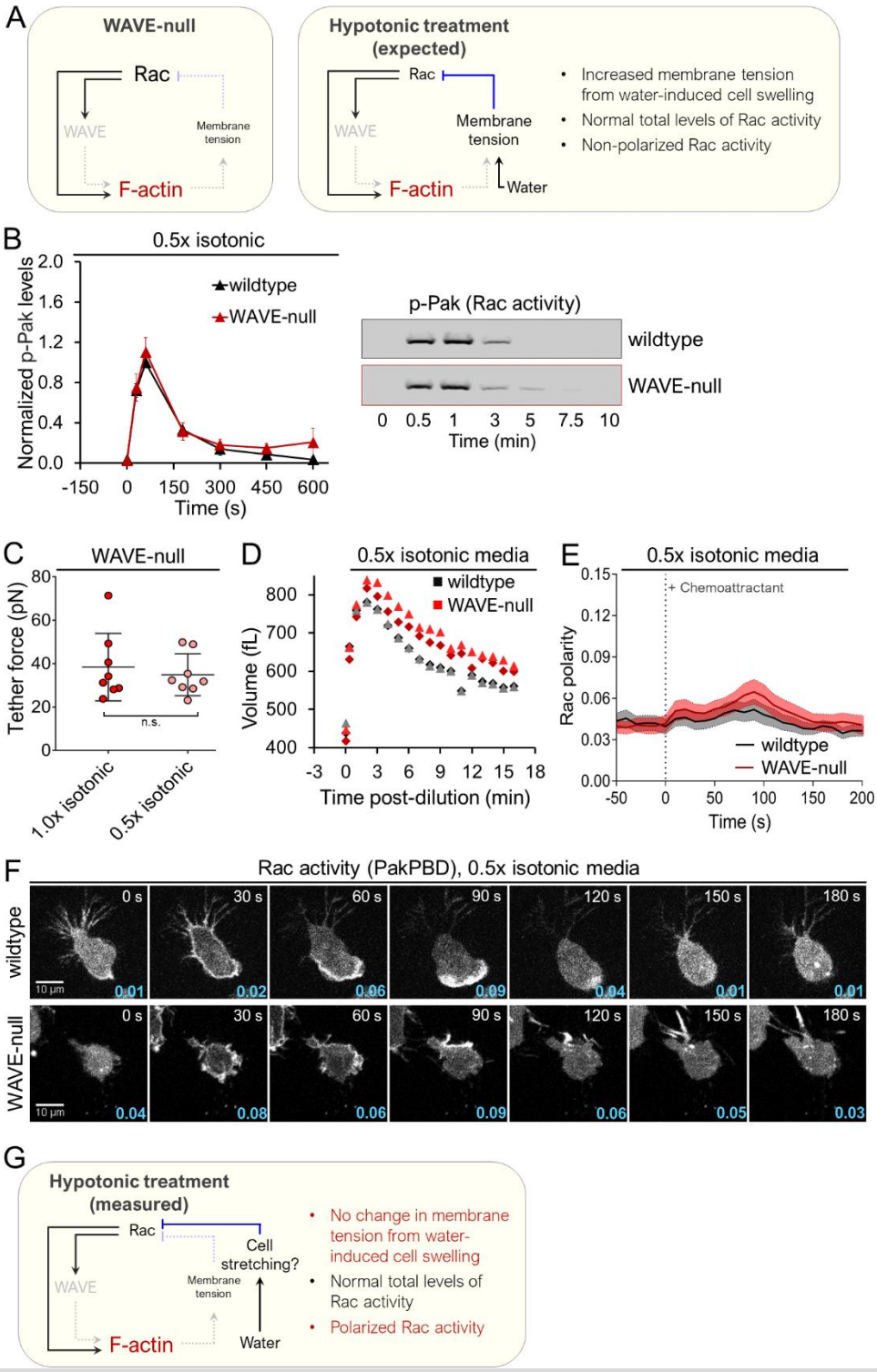

Figure 5. Hypotonic treatment to extend the plasma membrane restores spatiotemporal Rac activity in cells lacking WAVE complex.

A) Left, schematic depicting key components in the neutrophil polarity circuit and their measured alterations in WAVE-null cells. Right, expected regulatory changes among key polarity components in WAVE-null cells following hypotonic-induced plasma membrane stretching, where we hypothesized a rescue of Rac activity levels.

B) dHL-60s were suspended in 0.5x isotonic media, stimulated with 10 nM fMLP and samples were collected and processed for immunoblot. Left, Rac activity was quantified via phospho-Pak as in 3A. Each point represents an average of 4 independent experiments, with data for each experiment normalized to wildtype cells at '0 s'. Error bars, SEM. Right, representative immunoblot.

C) Membrane tether force of dHL-60s was measured using AFM as described in 2B. The same cells were measured before and after hypotonic shock. Note that the cells in the '1.0x' condition are a subset of the data depicted in 2B that were further subjected to hypotonic treatment. The data are reproduced here to aid comparison. Each point represents a single cell. Data were pooled from 2 independent experiments. Error bars, SD. Membrane tension does not significantly change following hypotonic shock.

D) Volumes of dHL-60 cells in suspension following 0.5x isotonic treatment were measured using a Coulter Counter. Each point represents the mode volume for a distribution of >7000 cells (see "Materials and Methods" for details). Data are pooled from 2 independent experiments. Volume significantly increases following hypotonic shock.

E) dHL-60 cells in 0.5x isotonic media expressing the Rac activity reporter PakPBD-mCitrine were imaged as in 3B. Values in cyan indicate the degree of Rac polarization, as described in 3D.

F) Quantification of Rac polarity as described in 3D for cells prepared as in C. Dark lines, mean polarity of Rac activity. Light shaded regions, +/- 95% CI of the mean. N = 148 wildtype and 129 WAVE-null cells pooled from 2 independent experiments.

G) Schematic depicting measured regulatory changes among key polarity components in WAVE-null cells following hypotonic treatment. Compare with expected changes in 5A.

WAVE complex is dispensable for polarization in confined environments

As hypotonic treatment has the potential to introduce pleiotropic effects beyond cell shape changes, we employed an orthogonal approach to stretch the plasma membrane using mechanical force. Using polydimethylsiloxane (PDMS)-based devices, we created confined environments where chamber height could be adjusted by applying vacuum (Le Berre et al., 2012). We observed neutrophil migration at two confinement regimes: 'weak', 5-9 μm chamber height; and 'strong', <5 μm chamber height. Acute stimulation of cells in this device was achieved using ultraviolet light to release chemically-caged chemoattractant (Collins et al., 2015; Pirrung et al., 2000) (**Fig. 6A**), and polarization of Rac activity was monitored using PakPBD. Wildtype cells under weak or strong confinement produced similar chemoattractant-based increases in polarized Rac activity (**Fig. 6B-C; Videos 7-8**). These responses broadly resembled those we observed in wildtype cells during unconfined migration (**Fig. 3B-C**).

Whereas unconfined WAVE-null cells failed to polarize Rac activity when stimulated, weak confinement partially rescued this defect (**Figs. 6D-E**), similar to our experiments in hypotonic media. Despite this increase in polarization, protrusion morphology remained finger-like (**Fig. 6D**, top row; **Video 9**) and the mean perimeter-to-area ratio remained high: 0.33 ± 0.01 μm^{-1} for wildtype cells vs. 0.42 ± 0.01 μm^{-1} for WAVE-null cells (**Fig. 6F**). Further increasing cell confinement gave a substantially more profound rescue of polarity and motility in WAVE-null cells. Cells switched from producing finger-like protrusions to generating smooth leading edges that much more closely resembled the overall shape of wildtype cells (**Fig. 6D**, bottom row; **Video 10**). Likewise, strongly-confined wildtype and WAVE-null cells showed identical mean perimeter-to-area ratios of 0.28 ± 0.01 μm^{-1} (**Fig. 6F**). These alterations in polarity and morphology were rapid

and reversible. Repeatedly raising and lowering the height of the chamber caused WAVE-null neutrophils to switch from generating clustered finger-like protrusions to making smooth protrusions (**Video 11**). Stimulation of these strongly-confined WAVE-null neutrophils resulted in pronounced polarization of Rac activity that was even more profound than wildtype cells under this degree of confinement (compare blue-dashed lines in **Figs. 6C and 6E**). We additionally observed chemokinesis in confined WAVE-null cells, finding that their motility was improved compared to unconfined WAVE-null cells. Over a 10-min observation period, confined WAVE-null cells showed a mean maximum displacement of 21 ± 1 μm from their initial positions vs. 14 ± 1 μm unconfined WAVE-null cells (**Fig. 6G**). Additional experiments performed in ARP2-null cells produced similar results (**Fig. 6H-I**), further underscoring that all branched actin assembly is dispensable for the short-range positive feedback that enables Rac polarity, leading edge morphology, and persistent motility.

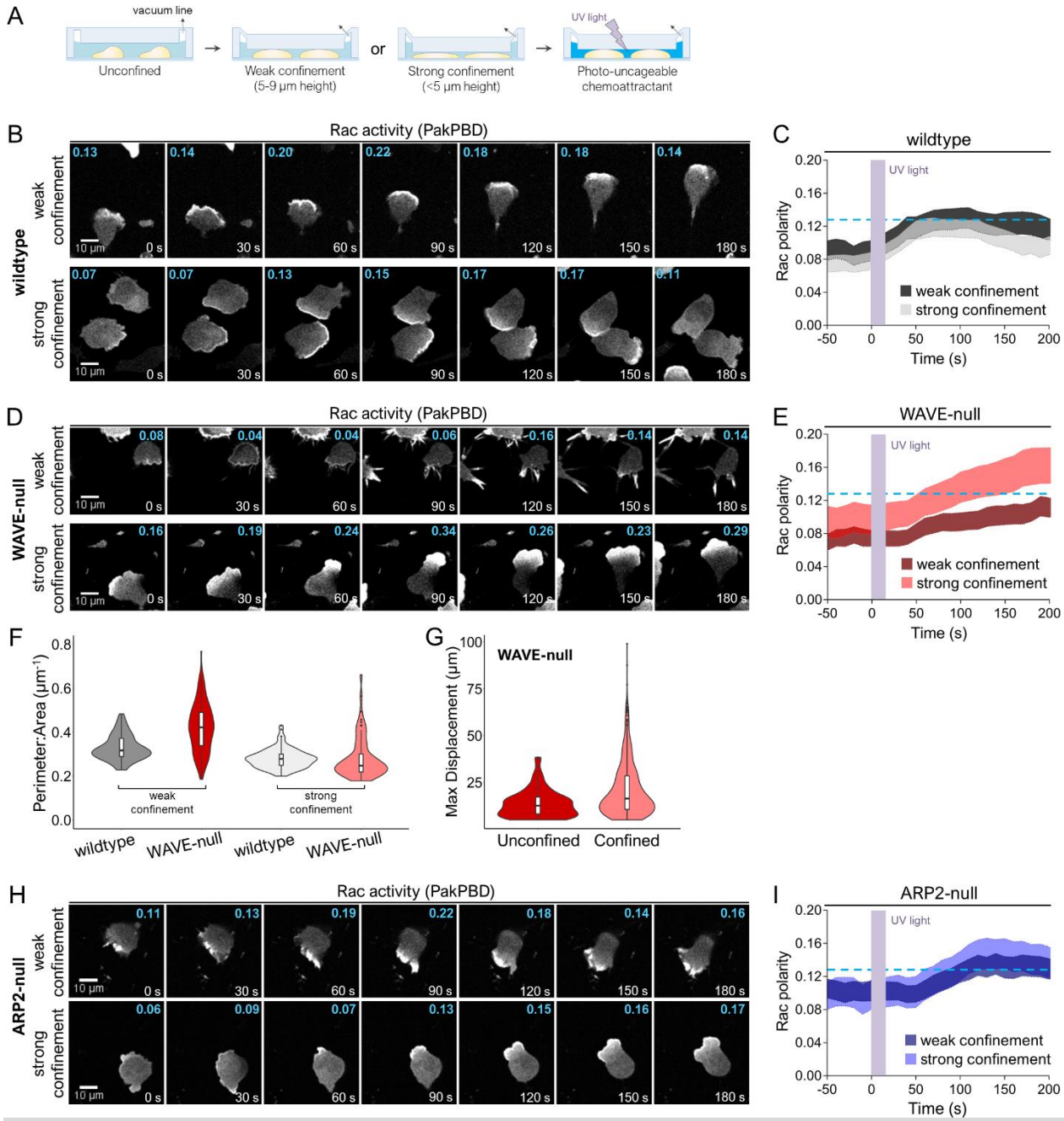

Figure 6. Cell compression restores polarization in cells lacking WAVE or Arp2/3 complex.

A) Schematic for cell confinement experiments. The height of the chamber was set using a vacuum regulator.

B, D, H) dHL-60 cells expressing the Rac biosensor PakPBD were plated on fibronectin-coated glass in media containing 10 µM caged-fMLP and imaged every 10 s by confocal microscopy. Chamber height was set as shown in A. Values in cyan indicate the degree of Rac activity polarization, as described in 3D, for the topmost cell fully inside each panel.

C, E, I) Quantification of Rac polarity as described in 3D for cells prepared as in A. Violet bars indicate when UV was used to photo-uncage caged-fMLP (0-20 s). Shaded regions, +/- 95% CI of the mean Rac polarity. **C)** N = 134 or 122 wildtype cells under strong or weak confinement, respectively, pooled from 5

independent experiments. **E)** N = 73 or 143 WAVE-null cells under strong or weak confinement, respectively, pooled from 3 independent experiments.

F) Perimeter-to-area ratios for cells prepared as in A. N = 58, 144, 93, or 73 weakly confined wildtype, weakly confined WAVE-null, strongly confined wildtype, or strongly confined WAVE-null cells, respectively, pooled from 2 independent experiments.

G) dHL-60s under "strong confinement" were prepared as in A. Cells were tracked using NucBlue nuclear stain and imaged every 10 s by confocal microscopy. Each point in the distribution represents the furthest a cell moved relative to its initial starting position over the 10-min observation period. N = 865 confined WAVE-null cells pooled from 2 independent experiments. Data for "unconfined" cells are replicated from 1E to aid in comparison.

I) N = 64 or 122 ARP2-null cells under strong or weak confinement, respectively, pooled from 2 independent experiments.

Polarization under confinement relies on bleb-like protrusions in the absence of WAVE

In addition to using actin-rich pseudopods for motility, migratory cells build bleb-based protrusions in certain microenvironments (Lämmermann and Germain, 2014; Paluch et al., 2016). These types of protrusions depend on high actomyosin contractility and occur when local weakening of membrane-to-cortex-attachments leads to the separation of the plasma membrane from the underlying actin cortex. Hydrostatic pressure then drives the expansion of this detached segment of membrane to form a protrusion initially lacking filamentous actin (Paluch and Raz, 2013). Upon preliminary inspection of WAVE-null cell movement under strong confinement, motility appeared to be powered by a bleb-based migration mode (**Video 10**). To probe if this mode of migration was dependent on the typical actomyosin drivers of blebbing, we treated neutrophils with the ROCK inhibitor Y27632 to block myosin contractility (Maugis et al., 2010). In other contexts, ROCK is required for blebbing but is dispensable for actin protrusion-based chemotaxis (Liu et al., 2015a). WAVE-null cells treated with Y27632 under strong confinement showed reduced polarization of Rac activity upon stimulation and formed only finger-like protrusions (**Fig. 7A-B**). Under weak confinement, where WAVE-null cells generally do not form bleb-like protrusions, treatment with Y27632 had minimal effect on polarization of Rac activity (**Fig. 7A-B**). Similarly, wildtype cells treated with Y27632 showed little change in polarized Rac activity, consistent with protrusion growth and cell movement being independent of myosin-based contractility in these cells (**Fig. 7C-D**). Our ROCK inhibition experiments show that the smooth protrusions formed by strongly-confined WAVE-null cells, like blebs, depend on myosin contractility.

The highly polarized Rac activity in strongly-confined WAVE-null cells suggested the presence of short-range positive feedback loops in maintaining localized protrusion growth. To explore this possibility further, we imaged cells expressing PakPBD with high temporal frequency to assess whether Rac activity correlated with growth of bleb-like protrusions. Intriguingly, the bleb-like protrusions we observed in WAVE-null cells occurred via processive extensions of the plasma membrane that travelled around the cell periphery. At regular intervals, the extension would reverse directions and form a highly-stereotyped serpentine pattern, confining processive extensions to a small section of the plasma membrane to form a leading edge (**Video 12**). This mode of protrusion resembles the long-known 'circus movements', where a bleb forms and

progressively extends around the cell in a clockwise or counter-clockwise direction (Loeb, 1928). However, circus movements only occasionally undergo direction reversals (Charras et al., 2008), whereas serpentine protrusions in strongly-confined WAVE-null neutrophils do so on the order of seconds, with these reversals seeming to maintain productive extension at the portion of the membrane containing high Rac activity (**Video 12**). We divided the plasma membrane into 1000 discrete segments and quantified both edge velocity and PakPBD fluorescence for each membrane segment over time (**Fig. 7E and Video 13**; see 'Methods' for details). Edge velocity and PakPBD showed an average instantaneous Pearson correlation coefficient of 0.17 (**Fig. 7F**). We next shifted the PakPBD intensity measurements for a given timepoint relative to the edge velocity measurements to assess whether local increases in Rac activity preceded or followed local increases in edge velocity. The correlation between PakPBD fluorescence and edge velocity was highest (Pearson correlation coefficient of 0.27) when PakPBD signal was shifted backwards in time by 6 s relative to edge velocity (**Fig. 7F**). This analysis indicates that the localized extension of bleb-like protrusions slightly precedes Rac activation, but that Rac activity may restrict the region of the plasma membrane that is permissive for protrusion extension. As these results are only correlative however, this relationship may arise as an indirect result of another related process (e.g., RhoA-dependent polarity establishment at the trailing edge (Xu et al., 2003)). Our data indicate that neutrophils employ mechanisms independent of branched actin assembly to enrich Rac activity at the leading-edge during bleb-based migration. Furthermore, the ability of strongly-confined WAVE-null cells to migrate exclusively using bleb-like protrusions may serve as a useful platform for dissecting the short-range positive feedback loops underlying bleb-based migration in future work.

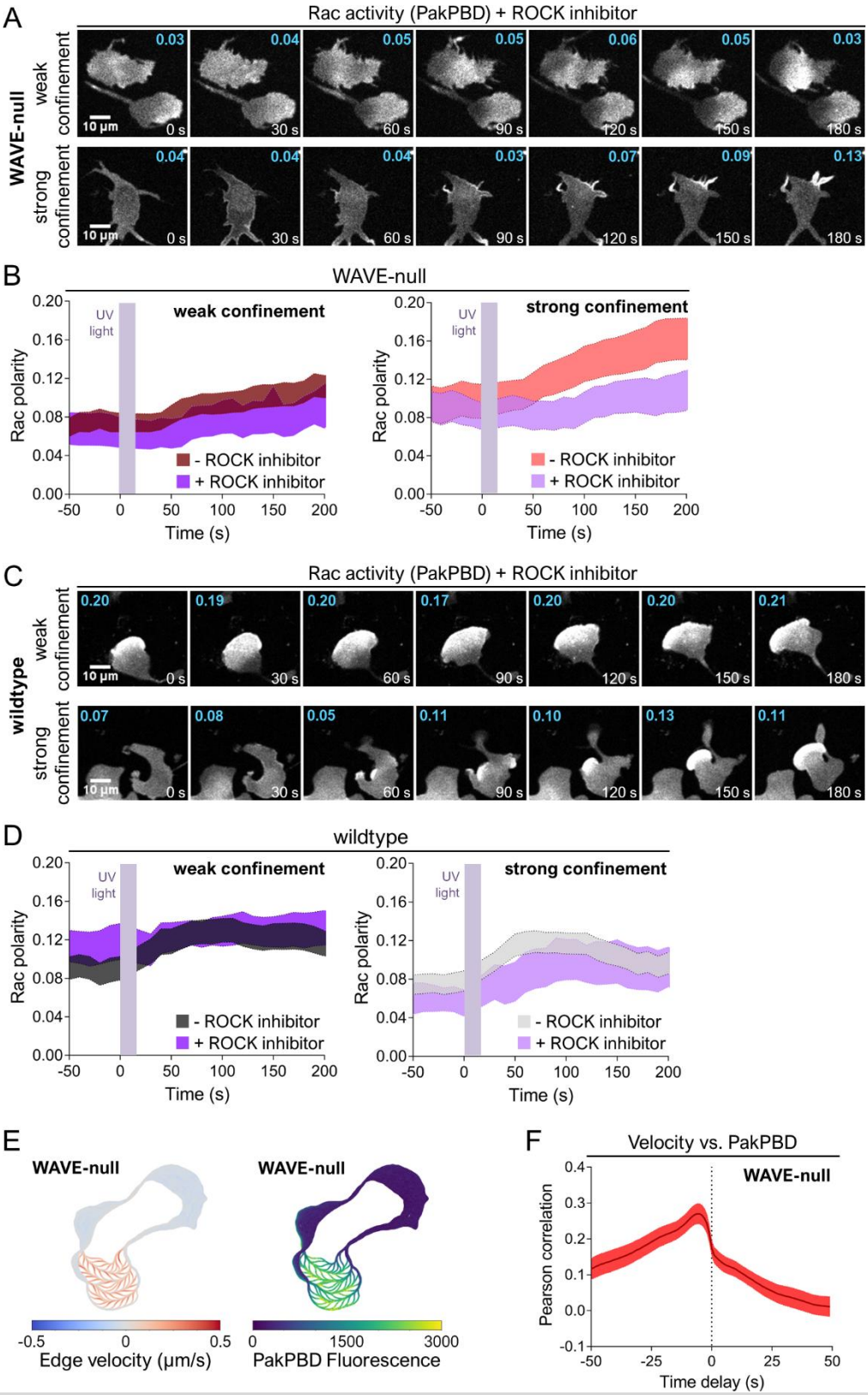

Figure 7. WAVE-null cells under 'strong' physical confinement migrate using bleb-like protrusions.

A, C) dHL-60 cells expressing the Rac biosensor PakPBD were plated on fibronectin-coated glass in media containing 10 µM caged-fMLP and 20 µM Y27632 and imaged as in 6B. Prior to imaging, cells were placed

under weak or strong confinement, as depicted in 6A. Values in cyan indicate the degree of Rac polarization, as described in 3C, for the topmost cell fully inside each panel.

B, D) Quantification of PakPBD polarity as described in 3C for cells prepared as in 6A. Violet bars indicate when UV was used to photo-uncage caged-fMLP (0-20 s). Light shaded regions, +/- 95% CI of the mean Rac polarity. **B)** N = 31 or 53 Y27632-treated WAVE-null cells under strong or weak confinement, respectively, pooled from 2 independent experiments. Data for "- ROCK inhibitor" cells are reproduced from 6E to aid in comparison. **D)** N = 53 or 43 Y27632-treated wildtype cells under strong or weak confinement, respectively, pooled from 2 independent experiments. Data for "- ROCK inhibitor" cells are reproduced from 6C to aid in comparison.

E) Overlays of extracted cell boundaries over time displaying associated edge velocity (left) and Pak-PBD edge fluorescence (right).

F) Analysis of Pearson correlation between edge velocity and Pak-PBD fluorescence as a function of temporal offset in fluorescence. The peak Pearson correlation occurs when fluorescence values of Rac activation are shifted back in time by approximately 6 seconds relative to membrane extension, suggesting that membrane extension precedes changes in local Rac activation by 6 seconds.

DISCUSSION

Polarization of migratory cells requires coordinated positive and negative feedback loops to restrict protrusion growth to a single site. Actin polymerization is thought to underlie both types of feedback (Diz-Muñoz et al., 2016; Huang et al., 2013; Inoue and Meyer, 2008; Sasaki et al., 2007; Wang et al., 2002; Weiner et al., 2007; Yang et al., 2016), but the roles of different types of actin networks in providing each kind of feedback have not been carefully addressed. Here, we show that branched actin assembly is dispensable for producing short-range positive feedback (**Fig. 6**), whereas the importance of actin in providing long-range negative feedback varies with microenvironment (compare **Figs. 3 and 4** with **Fig. 6**). These observations require a revision of the dominant view that branched actin assembly plays essential roles in both types of feedback.

For the long-range inhibition that enables fronts to compete with one another, our data show that this negative feedback can be induced by mechanical deformation of the plasma membrane (**Fig. 5**). When neutrophils migrate in unconfined environments, WAVE-dependent branched actin assembly is required for generating this force (**Figs. 1 and 2**). Computational simulations suggest that the ability of WAVE complex to increase tension and generate sheet-like protrusions may depend on its spatial patterning at the plasma membrane, which in turn depends on its curvature-dependent recruitment (**Figs. 2F and S3**). However, upon confinement, the resulting membrane extensions arising by this perturbation can compensate for the polymerization force normally provided by branched actin assembly (**Fig. 6**). This confinement puts WAVE-null cells in a regime where producing either finger-like actin-rich protrusions or bleb-like protrusions can now provide enough protrusive force to satisfy the long-range negative feedback requirement for polarity. How do cells read out these forces to constrain the levels and spatial distribution of leading-edge regulators? In previous work (Houk et al., 2012), we showed that membrane tension is likely to regulate this long-range inhibitor: Increasing membrane tension suffices to inhibit leading edge signals, whereas decreasing membrane tension prevents their restriction. However, it has been difficult to discern whether cells read out membrane tension directly or other correlated physical properties, such as cell shape or local membrane curvature. Here we leveraged mechanical

perturbations (i.e. mild hypotonic treatment) which rescue the ability of WAVE-null cells to constrain Rac activity. Importantly, these perturbations do not increase membrane tension despite causing significant changes to cell shape—up to a two-fold increase in volume (**Fig. 5**). These results disfavor mechanisms where mechanosensors restricting Rac activity only respond directly to membrane tension changes, suggesting that tension sensors such as stretch-activated ion channels (e.g., Piezo (Cox et al., 2016)), cannot be the sole class of mechanosensors mediating neutrophil long-range inhibition. Given that osmotically-induced swelling/shrinking leads to changes in membrane geometry (Cheung et al., 1982; Ting-Beall et al., 1993), mechanosensors respond to changes in membrane shape, using curvature-sensitive membrane binders like BAR proteins (Mim and Unger, 2012), are likely to be required.

Along with generating long-range negative feedback, actin assembly is thought to provide short-range positive feedback to enable polarity (Krause and Gautreau, 2014; Nguyen et al., 2016). However, assessing the role of actin assembly in positive feedback has been challenging. Much of this difficultly has stemmed from a lack of tools for decoupling actin's role in both types of feedback. Pharmacological inhibitors of actin polymerization like latrunculin target all actin networks and would be expected to break all actin-based feedback. Even our more focused approach of targeting only WAVE-dependent (**Figs. 1-3**) or Arp2/3-dependent (**Fig. 4**) actin assembly initially failed to provide this decoupling. It was only when we combined these genetic perturbations (i.e. knockout of *HEM1* or *ARP2*) with mechanical perturbations (to satisfy long-range negative feedback) that we were able to isolate and dissect the role of branched actin assembly in providing short-range positive feedback. This combined approach revealed that branched actin assembly is not required for short-range positive feedback, in contrast to the general assumptions in the field (Iglesias and Devreotes, 2012; Krause and Gautreau, 2014; Saha et al., 2018; Stanley et al., 2014).

When placed under strong confinement, cells lacking WAVE complex polarize and migrate using bleb-like protrusions (**Figs. 7A-D**). These observations are consistent with prior work showing that neutrophils and other migratory cells use distinct strategies to achieve migration in different external environments (Bergert et al., 2012; Liu et al., 2015b; Wilson et al., 2013; Yip et al., 2015). However, neutrophils migrating using this bleb-like mode strongly polarize Rac activity to a small section of the plasma membrane (**Fig. 6D-E**), and Rac activity coincides with protrusion formation and extension (**Fig. 7E-F**), suggesting a branched actin-independent feedback circuit organizing the local positive feedback circuit for Rac activity during this mode of migration. It is interesting that neutrophils may rely on the same Rac GTPase to organize motility around both actin-rich and bleb-like protrusions; this is not unique to neutrophils, as other cell types that migrate using blebs, such as zebrafish primordial germ cells (PGCs), rely on Rac activity to support bleb growth (Kardash et al., 2010). Bleb-based motility in PGCs also relies on Cdc42-dependent 'wrinkling' of the plasma membrane to create membrane reservoirs that can be released as blebs form and expand (Goudarzi et al., 2017). Since the Cdc42/WASP axis supports neutrophil polarity (Fritz-Laylin et al., 2017; Yang et al., 2016), it would be interesting to test whether this pathway contributes to membrane wrinkling in neutrophils. Such a mechanism would enable neutrophils

to extend large amounts of membrane stores when moving through complex microenvironments in vivo or to buffer themselves against changes in cell volume caused by fluctuations in osmolarity.

In summary, we used a combination of genetic and mechanical perturbations to show that branched actin assembly is not universally required for generating the positive and negative feedback loops needed to support neutrophil polarity and motility: The role of branched actin in these processes is strongly influenced by cell-extrinsic factors. By decoupling changes in membrane tension from cell volume, we further show that polarity-regulating mechanosensors are unlikely to respond directly to tension changes but may instead distinguish changes in membrane morphology. Comparing these experimental observations to our computational simulations predicts that the WAVE complex is associated with a high convex curvature, while the actin nucleators in the finger-like protrusions of WAVE-null cells have a very low spontaneous curvature. This prediction awaits future experimental verification. Going forward, leveraging well-defined environmental perturbations will be helpful in deconvolving the pleiotropic effects arising when disrupting components with multiple cellular functions. This strategy will be particularly important for dissecting processes such as directed migration, where a complex interplay between cell-intrinsic and cell-extrinsic factors underlies cell physiology.

MATERIALS AND METHODS

Cell culture. Performed essentially as previously described (Graziano et al., 2017). HL-60 cells were grown in RPMI 1640 media supplemented with L-glutamine and 25 mM HEPES (Corning) and containing 10% (v/v) heat-inactivated fetal bovine serum (Gibco). Cultures were maintained at a density of 0.2-1.0 million cells/mL at 37°C/5% CO_2. Differentiated HL-60 cells (dHL-60s) were obtained by adding 1.5% (v/v) DMSO (Sigma-Aldrich) to actively growing cells at a density of 0.3 million/mL followed by incubation for an additional 4-5 days. HEK293T cells (used to generate lentivirus for transduction of HL-60 cells) were grown in DMEM (Corning) containing 10% (v/v) heat-inactivated fetal bovine serum (Gibco) and maintained at 37°C/5% CO_2.

Plasmids. A vector for mammalian expression of PakPBD-mCitrine was generated by PCR amplification of previously-described PakPBD (Weiner et al., 2007) and mCitrine, and the PCR products were ligated into the pHR backbone between the MluI and NotI sites. Guide RNAs with homology to exon 5 of *NCKAP1L/HEM1* (5' TGTCACGGATTGAAGATCGG 3') and exon 1 of *ACTR2* (5' GGTGTGCGACAACGGCACCG 3') were cloned into the previously-described LentiGuide-Puro vector (Sanjana et al., 2014), Addgene plasmid #52963. A vector expressing human condon optimized *S. pyrogenes* Cas9-BFP was previously described (Graziano et al., 2017).

Transduction of HL-60 cells. Performed essentially as previously described (Graziano et al., 2017). HEK293T cells were seeded into 6-well plates and grown until ~80% confluent. For each well, 1.5 µg pHR vector (containing the appropriate transgene), 0.167 µg vesicular stomatitis virus-G vector, and 1.2 µg cytomegalovirus 8.91 vector were mixed and prepared for transfection using TransIT-293 Transfection Reagent (Mirus Bio) per the manufacturer's instructions. Following

transfection, cells were grown for an additional 3 days, after which virus-containing supernatants were harvested and concentrated ~40-fold using Lenti-X Concentrator (Clontech) per the manufacturer's instructions. Concentrated viruses were frozen and stored at -80°C until needed. For all transductions, thawed virus was mixed with ~0.3 million cells in growth media supplemented with polybrene (8 µg/mL) and incubated overnight. Cells expressing desired transgenes were isolated by culturing in growth media supplemented with puromycin (1 µg/mL) or using fluorescence-activated cell sorting (FACS) as appropriate (FACSAria2 or FACSAria3; BD Biosciences).

Generation of knockout cell lines using CRISPR/Cas9. Wildtype HL-60 cells were transduced with vectors containing puromycin-selectable guide RNAs (gRNAs) targeting *HEM1/NCKAPL1* or *ARP2/ACTR2*. Following selection, cells were then transduced with an *S. pyrogenes* Cas9 sequence fused to tagBFP. Cells expressing high levels of Cas9-tagBFP were collected using fluorescence-activated cell sorting (FACS), after which a heterogeneous population was obtained, as assessed by immunoblot and by sequencing of the genomic DNA flanking the Cas9 cut site. These cells were then diluted into 96-well plates at a density of ~1 cell per well to generate clonal lines, which were again verified by genomic DNA sequencing and immunoblot. We verified that candidate clonal lines arose from single cells as previously described (Graziano et al., 2017).

Preparation of dHL-60s for microscopy. For experiments where cells were observed in unconfined environments, 96-well #1.5 glass-bottom plates (Brooks Life Sciences) were coated with a 100 µL solution of 20 µg/mL porcine fibronectin (prepared from whole blood) and 11 mg/mL bovine serum albumin (BSA, endotoxin-free, fatty acid free; A8806, Sigma) dissolved in Dulbecco's Phosphate Buffered Saline (DPBS; 14190-144, Gibco) and incubated for 30 min at room temperature. The fibronectin solution was then aspirated, and each well was washed twice with 300 µL DPBS. For each well, 0.2-0.4 mL of dHL-60 cells in growth media were pelleted at 200 x g for 5 min, resuspended in 100 µL imaging media (Leibovitz's L-15 with 0.2% (w/v) BSA, 0.4 mM NaOH, and 1 nM fMLP) and plated. For experiments where PakPBD polarity was quantified (e.g., **Fig. 3B-C**) or where trajectories were measured (e.g., **Fig. 1D-E**), 5 µM CellTracker Red (C34552, Thermo Fisher) or 1 drop/500 mL NucBlue (R37605, Thermo Fisher), respectively, were added to the imaging media. Cells were then incubated at 37°C/5% CO_2 for >10 min to permit adherence to the glass, followed by one wash using 100 µL imaging media (containing neither CellTracker Red nor NucBlue dyes).

For experiment where cells were observed in confined environments (i.e. using PDMS-based devices), 25-mm round #1.5 glass coverslips were coated/incubated with a fibronectin/BSA solution (as described in the preceding paragraph), washed once with 1 mL DPBS, and once with 0.4 mL deionized water. Immediately prior to plating cells, coverslips were dried under gaseous N_2. For each coverslip, 0.2-0.4 mL of dHL-60s in growth media were pelleted at 200 x g for 5 min, resuspended in 20 µL imaging media with 5 µM CellTracker Red, plated, and incubated at 37°C/5% CO_2 for >10 min to permit adherence to the glass. Cells were then washed once using 50 µL imaging media (without CellTracker Red) and 20 µL imaging media with 10 µM nv-fMLP

(chemically caged fMLP, prepared as in (Collins et al., 2015)). PDMS devices (see next section for fabrication) were then placed on top of cells as depicted in **Fig. 6A**, leftmost panel.

Microscopy hardware. All imaging experiments with the exception of those depicted in **Figs. 1B, 1D-E, and 6G** were performed at 30°C on a Nikon Eclipse Ti inverted microscope equipped with a motorized laser total internal reflection fluorescence (TIRF) illumination unit, a Borealis beam conditioning unit (Andor), a CSU-W1 Yokugawa spinning disk (Andor), a 60X PlanApo TIRF 1.49 numerical aperture (NA) objective (Nikon), an iXon Ultra EMCCD camera (Andor), and a laser merge module (LMM5, Spectral Applied Research) equipped with 405, 440, 488, and 561-nm laser lines. All hardware was controlled using Micro-Manager (UCSF). For experiments performed under confinement, the PDMS devices were connected with PE 20 tubing (Braintree Scientific) to a vacuum regulator (IRV1000-01B, SMC Pneumatics) which, in turn, was connected to the building-wide vacuum supply. Experiments depicted in **Fig. 6G** were performed at 37°C, but using the same hardware as the others described in this paragraph.

Imaging experiments depicted in **Figs. 1B and 1D-E** were performed at 37°C on a Nikon Eclipse Ti inverted microscope equipped with a motorized stage (ASI), a Lamba XL Broad Spectrum Light Source (Sutter), 20x 0.75 NA Plan Apo and 60x 1.4 NA Plan Apo objectives (Nikon), and a Clara interline CCD camera (Andor). All hardware was controlled using Nikon Elements.

Imaging and analysis. ImageJ (NIH), CellProfiler (Broad Institute), RStudio, Excel (Microsoft), and Prism (Graphpad) were used for all image analysis.

For the displacement/trajectory measurements (e.g., **Fig. 1D-E**), NucBlue-labeled nuclei were imaged using a 20x objective and DAPI filter cube every 15 s for 10 min by widefield epifluorescence microscopy. The NucBlue channel was used to create a binary mask using Otsu's method, from which the individual nuclei were segmented. For each nucleus, the center of mass of its binary representation was calculated in each frame. Displacements were calculated by measuring center of each nucleus at each timepoint and calculating the distance from its starting point (i.e. at t = 0 s). Cells were omitted from analysis for the following reasons: i) entering or leaving the field of view during the 10-min observation window, ii) achieving a maximum displacement of < 5 μm during the 10-min observation window (i.e. to remove dead cells and debris), iii) undergoing collisions and/or forming clumps that prevented reliable segmentation of individual nuclei. For the trajectory plots depicted in **Fig. 1D**, the x-y coordinates of the nuclear positions were normalized to (0, 0) at '0 s'. All summary statistics described in the text are mean distance ± SEM.

For the polarity measurements (**Figs. 3B-C, 4D-E, 5E-F, 6B-E, 6H-I and 7A-D**), 488-nm and 561-nm lasers were used to image PakPBD-mCitrine and CellTracker Red, respectively, every 10 s for 5 min by spinning disk confocal microscopy. Focal planes were chosen to be in the lower half of the cell, just above the ventral surface. Cells were stimulated with chemoattractant (fMLP) immediately following the '60 s' timepoint. For experiments performed in 96-well plates (unconfined migration) in isotonic media (e.g., **Fig. 3B-C**), imaging media containing 0.2% BSA and 200 nM fMLP was added to cells 1:1 to yield a final concentration of 100 nM fMLP. For

experiments performed in 96-well plates in 0.5x isotonic media (**Fig. 5E-F**), cells were plated in imaging media as described in "Preparation of dHL-60s for microscopy". An equal volume of deionized water with 0.2% BSA and 1 nM fMLP was added to cells, followed by incubation for 10 min at 30°C. Afterwards, an equal volume imaging media containing 200 nM fMLP and 0.2% BSA was added to cells, yielding a final concentration of 100 nM. For experiments performed in PDMS devices (confined migration), a 365-nm UV LED flashlight (Americans' Preferred) was used to photo-uncage nv-fMLP by holding the end of the flashlight 3-5 mm above the top of the PDMS chamber for ~15 s. Prior to each experiment, the power output of the flashlight was measured using a Slim Photodiode Power Sensor (S130C, Thor Labs). Flashlight batteries were replaced when the power output dropped below ~70% of the initial reading. Prior to analysis, all images were background-subtracted using a 'dark' image acquired by blocking all light from reaching the camera and averaging 100 exposures. The CellTracker Red channel was then used to create binary masks of the cell bodies using Otsu's method and each cell body was eroded inward by ~1 μm. Cell bodies were tracked as described in the preceding paragraph to account for cell movement during the experiment. At each timepoint, the cell bodies were used as seeds to identify the PakPBD-mCitrine signal associated with each cell using a previously-described propagation algorithm (Jones et al., 2005). The distance *(d)* between the center of mass of the PakPBD-mCitrine signal (weighted by fluorescence intensity) and the center of mass of a congruent PakPBD binary image (representing the cell's 'footprint') were calculated for each cell at each timepoint. To normalize for differences in cell cross-sectional area, the length *(L)* of the major axis of an ellipse that had the same normalized second central moments as the cellular PakPBD signal was determined. The distance d was then divided by $0.5L$, as depicted in **Fig. 3D**, to obtain a PakPBD polarity score ranging from 0 to ~1. In all experiments, polarity was quantified at every 10-s interval (beginning at 50 s prior to stimulation with chemoattractant) with the following exception: In experiments where UV light was used to un-cage nv-fMLP, data from the '10 s' and '20 s' timepoints were always omitted due to excessive background cause by UV light (omitted data indicated by violet bars in **Figs. 6C, 6E, 6I, 7B, and 7D**). Cells were omitted from analysis for the following reasons: i) touching the edge of the field of view during the 5-min observation window, ii) undergoing collisions and/or forming clumps that prevented reliable segmentation of individual cell bodies or PakPBD signal, iii) failure to express sufficiently high levels of PakPBD-mCitrine to permit reliable segmentation of cell outlines. In parallel, perimeter-to-area ratios for these same cells (e.g., **Fig. 1C**) were determined using binary representations of PakPBD signal for each cell. For individual cells, the ratios at 60, 70, 80, and 90 s following stimulation were averaged to obtain a single ratio. All summary statistics described in the text are mean ratio ± SEM.

For edge velocity and PakPBD fluorescence measurements (**Fig. 7E-F**), images were acquired every 1 s for 5 min. Background-corrected PakPBD images were segmented using a three-step process consisting of Gaussian smoothing, intensity-based thresholding, and distance-transform-based erosion. The threshold and degree of erosion were chosen manually to account for differences in the intensity and polarization of the biosensor in fluorescence images to align the boundary of the binary image with the apparent edge of the cell. To facilitate temporal analysis of

edge properties, these boundaries were then fit using a spline interpolation consisting of 1000 evenly-spaced points. The indices of points over time were aligned to minimize the Euclidean distance between point sets in space between consecutive time points. This approach allowed for relatively smooth tracking of points along the cell boundary, making temporal comparisons possible (this approach is conceptually similar to a previously-described alignment strategy (Huang et al., 2013)).

Edge velocity at a particular point *P* at time *t* was tracked by calculating the average of the distance transforms of the binary images at times *t-1* and *t+1* and interpolating the value of the signed distance transform at the coordinates of *P*. Edge fluorescence was tracked by interpolating the value of the background-corrected fluorescence image at the coordinates of *P*. Following alignment of the indices of the points, a temporal comparison of protrusion velocity and background-corrected fluorescence was analyzed by Pearson's cross-correlation function. Per-cell correlation functions were then averaged over multiple cells to give **Fig. 7F** as previously done (Machacek et al., 2009).

Atomic force microscopy. Custom-made chambers were coated for 30 min with fibronectin (prepared as described in the preceding section) and washed once with DPBS. dHL-60s were plated on each dish in growth media and allowed to adhere for at least 10 min at 37°C. After, cells were washed with RPMI supplemented with 2% FBS and 10 nM fMLP (experiments in **Fig. 4B**) or RPMI supplemented with 0.2% BSA and 10 nM fMLP (experiments in **Figs. 2B and 5C**).

Experiments in **Fig. 4B** were performed essentially as previously described (Diz-Muñoz et al., 2016). Olympus BioLevers (k = 60 pN/nm) were calibrated using the thermal noise method and incubated in 2.5 mg/ml Concanavalin A (C5275, Sigma) for 1 h at room temperature. Before the measurements, cantilevers were rinsed in DPBS. Tethers were pulled using a Bruker Catalyst AFM controlled by custom-made LabVIEW software mounted on an inverted Zeiss fluorescent microscope. Approach velocity was set to 1 μm/s, contact force to 100 pN, contact time to 5–10 s and retraction speed to 10 μm/s. After a 10 μm tether was pulled, the cantilever position was held constant until it broke. Tethers that took longer than 15 s to break were omitted from analysis as actin polymerized inside of these longer-lived tethers. Resulting force–time curves were analyzed with the Kerssemakers algorithm (Kerssemakers et al., 2006).

Experiments in **Figs. 2B and 5C** were performed as follows. Olympus BioLevers (k = 60 pN/nm) were calibrated using the thermal noise method and incubated in 2.5 mg/ml Concanavalin A (C5275, Sigma) for 1 h at room temperature. Before the measurements, cantilevers were rinsed in DPBS. Cells were located by brightfield imaging, and the cantilever was positioned at any location over the cell for tether measurement. Cells were not used longer than 1 h for data acquisition. Tethers were pulled using a CellHesion 200 from JPK mounted on an inverted Nikon Ti microscope. Approach velocity was set to 1 μm/s, contact force to 100-300pN, contact time to 5–10 s and retraction speed to 10 μm/s. After a 10 μm tether was pulled, the cantilever position was held constant until it broke. Negative and positive forces relate to the angle the cantilever takes, but the sign is arbitrary. By convention, contacting the cell deflects the cantilever towards positive values. Conversely, when the cantilever is pulled downwards by a membrane tether, the

values are negative. For experiments involving hypotonic treatment (**Fig. 5C**), tether force was first measured in cells plated in RPMI with 0.2% BSA and 10 nM fMLP. An equal volume of deionized water with 0.2% BSA and 10 nM fMLP was then added to the cells and tether force in these same cells was measured over a period of 3-15 min following water addition. Analysis of force-time curves was performed using the JPKSPM Data Processing Software.

Volume measurements. dHL-60s were pelleted at 180 x g for 5 min and resuspended at a density of ~20,000 cells/mL in RPMI supplemented with 1 nM fMLP. Volumes were measured using a Beckman Coulter Z2 Coulter Counter with a 100-micron aperture probe. The following settings were used: a calibration factor (Kd) of 59.96, a resolution of 256, a gain of 64, and a current of 0.354 mA. Samples of 0.5 mL were measured for each indicated timepoint. At timepoint '0 min', an equal volume of deionized water with 1nM fMLP was added to the sample, and cell volumes were measured at 1-min intervals for 16 min. For each interval, at least 7,000 cells were measured. A Gaussian function was fitted to each volume distribution to determine the mode volume for the time interval. Analysis was performed using SciDAVis.

Details of the simulations. The Monte-Carlo simulations of the membrane shape provided in this work follow the scheme described in (Fošnarič et al., 2013). The membrane is described as a triangulated surface, with each node representing either a membrane or a protein domain. In this work a network is composed of 3127 nodes, forming a network of approximately 6250 triangles. Nodes can move and bonds can flip according to the Monte-Carlo (Metropolis) algorithm, within the fixed topology of a sphere and with distance between nodes limited between minimal and 1.7 times larger value. The system is initially thermalized. This gives a thermally fluctuating self-avoiding membrane in steady-state, where protein domains are free to laterally diffuse within the membrane. The energy term due to tension is $W_A = \frac{k_A}{2}\sum_{i=1}^{N_t}(\frac{a_i}{a_0} - 1)^2$ where k_A is the elastic constant of the membrane and the sum runs over all of N_t triangles of the network, a_i is area of triangle i, and a_0 is area of a tensionless triangle. For a_0 we choose an equilateral triangle, $a_0 = \sqrt{3}l_0^2/4$, with side lengths $l_0 = (l_{min} + l_{max})/2$. We define membrane tension as the average tension per membrane area, $\sigma = \langle\frac{W_A}{A}\rangle$, where A is the area of the membrane for a given microstate and brackets denote the canonical ensemble average. In addition to the standard bending energy of the membrane, there is an energy term that describes the binding between neighboring proteins, with contact energy w, as well as an active force of magnitude F that acts at every protein node towards the outwards normal. **Figs. 2F** and **S3**, show results for a membrane at temperature $T/T_0 = 0.7$ with $\rho = 11\%$ of active proteins with protrusive force $F = 1kT_0/l_{min}$ and direct interaction constant $w = 1kT_0$. Elastic constants (k_A) of $1kT_0$ and $10kT_0$ are depicted in **Figs. 2F** and **S3**, respectively.

F-actin staining. For flow cytometry experiments, dHL-60s 4-5 days post-differentiation were concentrated to 1.5 million cells/mL and incubated in starvation media (serum-free RPMI 1640) for 45-60 min at 37°C/5% CO_2. Cells were stimulated in suspension using 100 nM fMLP, and, at indicated timepoints, 0.5 mL of cells were fixed by the addition of 0.5 mL "fixation buffer" (280 mM KCl, 2 mM $MgCl_2$, 4 mM EGTA, 40 mM HEPES, 0.4% bovine serum albumin (BSA), 640 mM

sucrose, 7.4% formaldehyde (w/v), pH 7.5) and incubated at room temperature for 15-20 min. For actin turnover experiments (**Fig. S2B**), cells were stimulated with 100 nM fMLP for 10 min, followed by addition of 50 nM Latrunculin B. Samples were collected at indicated timepoint, mixed 1:1 with "fixation buffer" and incubated at room temperature for 15-20 min. Cells were then pelleted, washed once with "intracellular buffer" (140 mM KCl, 1 mM $MgCl_2$, 2 mM EGTA, 20 mM HEPES, 0.2% BSA, pH 7.5), and resuspended in "staining buffer" (intracellular buffer + 130 nM rhodamine-phalloidin (ThermoFisher) and 0.2% Triton X-100). Following incubation at room temperature for 45 min, cells were pelleted and then resuspended in intracellular buffer. Cells were then stored at 4°C until immediately prior to flow cytometry analysis. Flow Cytometry data were collected on a FACSAria2 or FACSAria3 using FACSDiva software (BD Biosciences) and analyzed using Flowing Software 2.5 (http://flowingsoftware.btk.fi/). For each experiment, all fluorescence values were normalized to wildtype cells at '0 s'. All summary statistics described in the text are mean percentage ± SEM.

For microscopy experiments, cells were plated in 96-well glass-bottom plates as described in "Preparation of dHL-60s for microscopy" and stimulated using 100 nM fMLP. At indicated timepoints, an equal volume of "fixation buffer" was added to each well and cells were incubated at room temperature for 15-20 min. The fixation solution was then aspirated from each well, cells were washed once with "intracellular buffer", and 100 µL "staining buffer" was added to each well. Following incubation at room temperature for 45 min, the staining buffer was aspirated from each well, cells were washed once with "intracellular buffer" and 100 µL intracellular buffer was added to each well. Cells were stored at 4°C until immediately prior to imaging.

Fabrication of PDMS devices for cell confinement. PDMS devices were manufactured by mixing Sylgard 184 Silicone Elastomer Base and Sylgard 184 Elastomer Curing Agent (#4019862, Dow Corning) 10:1 (w/w), followed by degassing under vacuum. The exterior suction cup portion of the device was created by placing 3 aluminum rings on a clean silicon wafer in the following order to create concentric circles: i) a disc of 14 mm diameter and 0.5 mm height, ii) a ring of 8 mm inner diameter, 14 mm outer diameter, and 5 mm height, iii) a ring of 19 mm inner diameter, 40 mm outer diameter, and 7 mm height. Degassed PDMS mixture was poured into this mold, a glass slide was used to scape excess off the top, and the device was baked at 80°C for 1 h. Following removal of the device from the metal ring assembly, a 0.75 mm biopsy punch was used to create a hole in the top of the device where vacuum tubing could be inserted.

The second part of the device was fabricated using a silicon wafer with a regularly repeating array of micropillars (440 µm diameter, 5 µm height, spaced 1 mm apart; as previously described (Liu et al., 2015b)). Degassed PDMS mixture was poured onto the wafer, circular #1.5 coverslips (10 mm diameter) were pressed over top of these patterns using tweezers, and these assemblies were baked at 80°C for 1 h. A metal spatula and polyethylene cell lifters (#3008, Costar) were used to remove the PDMS-coated coverslips from the silicon wafer and these coverslips were subsequently attached to the central pillar of the suction cup portion of the device, glass side first. Devices were cleaned by sonication in 70% ethanol for 20 min and placed in a 37°C oven to dry. This cleaning procedure was performed each time a PDMS device was used for an experiment.

phospho-Pak timecourses. Performed essentially as previously described (Graziano et al., 2017): dHL-60s (4-5 days post-differentiation) were serum-starved by incubation in starvation media (growth media lacking fetal bovine serum) for 45-60 min at 37°C/5% CO_2 at a density of $1.5x10^6$ cells/mL. For hypotonic treatment experiments (**Fig. 5B**), cells were then diluted 1:1 using deionized water and incubated for an additional 10 min. Cells were next stimulated with 10 nM fMLP and samples were collected at indicated timepoints by mixing 0.5 mL of cells with 0.5 mL ice-cold stop solution (20% (w/v) trichloroacetic acid (TCA), 40 mM NaF, 20 mM β-glycerophosphate). Samples were incubated at 4°C for 1-12 hours, after which proteins were pelleted, washed once with 0.7 mL ice-cold 0.5% (w/v) TCA, and solubilized in 2x Laemmli sample buffer (Bio-rad). All timecourses were performed at ~25°C. Samples prepared for validating CRISPR-mediated gene editing (i.e. **Fig. S1**) were similarly prepared using TCA precipitation.

Immunoblot assays. Performed essentially as previously described (Graziano et al., 2017): Protein samples in 2x Laemmli sample buffer (prepared from 0.5-1.0 million cells) were subjected to SDS-PAGE, followed by transfer onto nitrocellulose membranes. Membranes were blocked for ~1 hr in a 1:1 solution of TBS (20 mM Tris, 500 mM NaCl, pH 7.4) and Odyssey Blocking Buffer (LI-COR) followed by overnight incubation at 4 °C with primary antibodies diluted 1:1000 in a solution of 1:1 TBST (TBS + 0.2% w/v Tween 20) and Odyssey Blocking Buffer. Membranes were then washed 3x with TBST and incubated for 45 min at room temperature with secondary antibodies diluted 1:15,000 in Odyssey Blocking Buffer. Membranes were then washed 3x with TBST, 1x with TBS and imaged using an Odyssey Fc (LI-COR). Analysis was performed using Image Studio (LI-COR) and Excel. For phospho-Pak immunoblots, the ratio of phospho-Pak to total Pak was calculated. These values were then normalized by scaling each relative to the value of wildtype cells at timepoint '0.5 min' for cells stimulated with chemoattractant.

Primary antibodies used were Phospho-PAK1 (Ser199/204)/PAK2 (Ser192/197) (Cell Signaling #2605), PAK2 (3B5) (Cell Signaling #4825), WAVE2 (Cell Signaling #3659), Arp2 (GeneTex #GTX103311), β-actin (Cell Signaling #3700), and GAPDH Loading Control Antibody (GA1R) (ThermoFisher). Secondary antibodies used were IRDye 680RD Goat anti-Mouse (Li-cor) and IRDye 800CW Goat anti-Rabbit (Li-cor).

ACKNOWLEDGEMENTS

We thank Alex Groisman, Pooja Suresh, Anne Pipathsouk, and Martin Bergert for experimental assistance, Sean Collins for providing photo-caged chemoattractant, members of the Weiner Lab for helpful discussions, and Kirstin Meyer for a critical reading of the manuscript. Support for this work was provided by a Cancer Research Institute Irvington Postdoctoral Fellowship to B.R.G., the NIH (GM118167 to O.D.W. and T32HL773125 to B.R.G.), the NSF Graduate Research Fellowship Program (Grant No. 1650113 J.P.T. and T.L.N.), the UCSF Moritz-Heyman Discovery Fellowship Program (T.L.N.), the Novo Nordisk Foundation (O.D.W.) and the Center for Cellular Construction (DBI-1548297), an NSF Science and Technology Center. The research work of M.F., S.P., A.I. and V.K.-I. was supported in part by the SI Research Agency (ARRS) grants No. J5-7098,

J1-6728 and P2-0232. N.S.G. is the incumbent of the Lee and William Abramowitz Professorial Chair of Biophysics. This study was also supported in part by HDFCCC Laboratory for Cell Analysis Shared Resource Facility through a grant from NIH (P30CA082103).

REFERENCES

Beli, P., Mascheroni, D., Xu, D., and Innocenti, M. (2008). WAVE and Arp2/3 jointly inhibit filopodium formation by entering into a complex with mDia2. Nat. Cell Biol. *10*, 849–857.

Bergert, M., Chandradoss, S.D., Desai, R.A., and Paluch, E. (2012). Cell mechanics control rapid transitions between blebs and lamellipodia during migration. Proc. Natl. Acad. Sci. USA *109*, 14434–14439.

Le Berre, M., Aubertin, J., and Piel, M. (2012). Fine control of nuclear confinement identifies a threshold deformation leading to lamina rupture and induction of specific genes. Integr Biol (Camb) *4*, 1406–1414.

Bieling, P., Hansen, S.D., Akin, O., Li, T.-D., Hayden, C.C., Fletcher, D.A., and Mullins, R.D. (2018). WH2 and proline-rich domains of WASP-family proteins collaborate to accelerate actin filament elongation. EMBO J. *37*, 102–121.

Blagg, S.L., Stewart, M., Sambles, C., and Insall, R.H. (2003). PIR121 regulates pseudopod dynamics and SCAR activity in Dictyostelium. Curr. Biol. *13*, 1480–1487.

Charras, G.T., Coughlin, M., Mitchison, T.J., and Mahadevan, L. (2008). Life and times of a cellular bleb. Biophys. J. *94*, 1836–1853.

Cheung, R.K., Grinstein, S., Dosch, H.M., and Gelfand, E.W. (1982). Volume regulation by human lymphocytes: characterization of the ionic basis for regulatory volume decrease. J. Cell Physiol. *112*, 189–196.

Collins, S.R., Yang, H.W., Bonger, K.M., Guignet, E.G., Wandless, T.J., and Meyer, T. (2015). Using light to shape chemical gradients for parallel and automated analysis of chemotaxis. Mol. Syst. Biol. *11*, 804.

Cox, C.D., Bae, C., Ziegler, L., Hartley, S., Nikolova-Krstevski, V., Rohde, P.R., Ng, C.-A., Sachs, F., Gottlieb, P.A., and Martinac, B. (2016). Removal of the mechanoprotective influence of the cytoskeleton reveals PIEZO1 is gated by bilayer tension. Nat. Commun. *7*, 10366.

Dai, J., and Sheetz, M.P. (1995). Regulation of endocytosis, exocytosis, and shape by membrane tension. Cold Spring Harb. Symp. Quant. Biol. *60*, 567–571.

Devreotes, P.N., Bhattacharya, S., Edwards, M., Iglesias, P.A., Lampert, T., and Miao, Y. (2017). Excitable signal transduction networks in directed cell migration. Annu. Rev. Cell Dev. Biol. *33*, 103–125.

Diz-Muñoz, A., Fletcher, D.A., and Weiner, O.D. (2013). Use the force: membrane tension as an organizer of cell shape and motility. Trends Cell Biol. *23*, 47–53.

Diz-Muñoz, A., Thurley, K., Chintamen, S., Altschuler, S.J., Wu, L.F., Fletcher, D.A., and Weiner, O.D. (2016). Membrane Tension Acts Through PLD2 and mTORC2 to Limit Actin Network Assembly During Neutrophil Migration. PLoS Biol. *14*, e1002474.

Fošnarič, M., Iglič, A., Kroll, D.M., and May, S. (2013). Monte Carlo simulations of a polymer confined within a fluid vesicle. Soft Matter *9*, 3976.

Fritz-Laylin, L.K., Lord, S.J., and Mullins, R.D. (2017). WASP and SCAR are evolutionarily conserved in actin-filled pseudopod-based motility. J. Cell Biol. *216*, 1673–1688.

Gauthier, N.C., Fardin, M.A., Roca-Cusachs, P., and Sheetz, M.P. (2011). Temporary increase in plasma membrane tension coordinates the activation of exocytosis and contraction during cell spreading. Proc. Natl. Acad. Sci. USA *108*, 14467–14472.

Goudarzi, M., Tarbashevich, K., Mildner, K., Begemann, I., Garcia, J., Paksa, A., Reichman-Fried, M., Mahabaleshwar, H., Blaser, H., Hartwig, J., et al. (2017). Bleb Expansion in Migrating Cells Depends on Supply of Membrane from Cell Surface Invaginations. Dev. Cell *43*, 577–587.e5.

Graziano, B.R., Gong, D., Anderson, K.E., Pipathsouk, A., Goldberg, A.R., and Weiner, O.D. (2017). A module for Rac temporal signal integration revealed with optogenetics. J. Cell Biol. *216*, 2515–2531.

Hallett, M.B., von Ruhland, C.J., and Dewitt, S. (2008). Chemotaxis and the cell surface-area problem. Nat. Rev. Mol. Cell Biol. *9*, 662; author reply 662.

Houk, A.R., Jilkine, A., Mejean, C.O., Boltyanskiy, R., Dufresne, E.R., Angenent, S.B., Altschuler, S.J., Wu, L.F., and Weiner, O.D. (2012). Membrane tension maintains cell polarity by confining signals to the leading edge during neutrophil migration. Cell *148*, 175–188.

Huang, C.-H., Tang, M., Shi, C., Iglesias, P.A., and Devreotes, P.N. (2013). An excitable signal integrator couples to an idling cytoskeletal oscillator to drive cell migration. Nat. Cell Biol. *15*, 1307–1316.

Iglesias, P.A., and Devreotes, P.N. (2012). Biased excitable networks: how cells direct motion in response to gradients. Curr. Opin. Cell Biol. *24*, 245–253.

Inoue, T., and Meyer, T. (2008). Synthetic activation of endogenous PI3K and Rac identifies an AND-gate switch for cell polarization and migration. PLoS One *3*, e3068.

Jones, T.R., Carpenter, A., and Golland, P. (2005). Voronoi-Based Segmentation of Cells on Image Manifolds. In Computer Vision for Biomedical Image Applications, Y. Liu, T. Jiang, and C. Zhang, eds. (Berlin, Heidelberg: Springer Berlin Heidelberg), pp. 535–543.

Kardash, E., Reichman-Fried, M., Maître, J.-L., Boldajipour, B., Papusheva, E., Messerschmidt, E.-M., Heisenberg, C.-P., and Raz, E. (2010). A role for Rho GTPases and cell-cell adhesion in single-cell motility in vivo. Nat. Cell Biol. *12*, 47–53; sup pp 1.

Keren, K., Pincus, Z., Allen, G.M., Barnhart, E.L., Marriott, G., Mogilner, A., and Theriot, J.A. (2008). Mechanism of shape determination in motile cells. Nature *453*, 475–480.

Kerssemakers, J.W.J., Munteanu, E.L., Laan, L., Noetzel, T.L., Janson, M.E., and Dogterom, M. (2006). Assembly dynamics of microtubules at molecular resolution. Nature *442*, 709–712.

Knaus, U.G., and Bokoch, G.M. (1998). The p21Rac/Cdc42-activated kinases (PAKs). Int. J. Biochem. Cell Biol. *30*, 857–862.

Krause, M., and Gautreau, A. (2014). Steering cell migration: lamellipodium dynamics and the regulation of directional persistence. Nat. Rev. Mol. Cell Biol. *15*, 577–590.

Kunda, P., Craig, G., Dominguez, V., and Baum, B. (2003). Abi, Sra1, and Kette control the stability and localization of SCAR/WAVE to regulate the formation of actin-based protrusions. Curr. Biol. *13*, 1867–1875.

Lämmermann, T., and Germain, R.N. (2014). The multiple faces of leukocyte interstitial migration. Semin Immunopathol *36*, 227–251.

Leithner, A., Eichner, A., Müller, J., Reversat, A., Brown, M., Schwarz, J., Merrin, J., de Gorter, D.J.J., Schur, F., Bayerl, J., et al. (2016). Diversified actin protrusions promote environmental exploration but are dispensable for locomotion of leukocytes. Nat. Cell Biol. *18*, 1253–1259.

Lieber, A.D., Yehudai-Resheff, S., Barnhart, E.L., Theriot, J.A., and Keren, K. (2013). Membrane tension in rapidly moving cells is determined by cytoskeletal forces. Curr. Biol. *23*, 1409–1417.

Litschko, C., Linkner, J., Brühmann, S., Stradal, T.E.B., Reinl, T., Jänsch, L., Rottner, K., and Faix, J. (2017). Differential functions of WAVE regulatory complex subunits in the regulation of actin-driven processes. Eur. J. Cell Biol. *96*, 715–727.

Liu, X., Yang, T., Suzuki, K., Tsukita, S., Ishii, M., Zhou, S., Wang, G., Cao, L., Qian, F., Taylor, S., et al. (2015a). Moesin and myosin phosphatase confine neutrophil orientation in a chemotactic gradient. J. Exp. Med. *212*, 267–280.

Liu, Y.-J., Le Berre, M., Lautenschlaeger, F., Maiuri, P., Callan-Jones, A., Heuzé, M., Takaki, T., Voituriez, R., and Piel, M. (2015b). Confinement and low adhesion induce fast amoeboid migration of slow mesenchymal cells. Cell *160*, 659–672.

Loeb, L. (1928). Amoebocyte tissue and amoeboid movement. Protoplasma *4*, 596–625.

Machacek, M., Hodgson, L., Welch, C., Elliott, H., Pertz, O., Nalbant, P., Abell, A., Johnson, G.L., Hahn, K.M., and Danuser, G. (2009). Coordination of Rho GTPase activities during cell protrusion. Nature *461*, 99–103.

Machesky, L.M., and Insall, R.H. (1998). Scar1 and the related Wiskott-Aldrich syndrome protein, WASP, regulate the actin cytoskeleton through the Arp2/3 complex. Curr. Biol. *8*, 1347–1356.

Machesky, L.M., Mullins, R.D., Higgs, H.N., Kaiser, D.A., Blanchoin, L., May, R.C., Hall, M.E., and Pollard, T.D. (1999). Scar, a WASp-related protein, activates nucleation of actin filaments by the Arp2/3 complex. Proc. Natl. Acad. Sci. USA *96*, 3739–3744.

Manser, E., Leung, T., Salihuddin, H., Zhao, Z.S., and Lim, L. (1994). A brain serine/threonine protein kinase activated by Cdc42 and Rac1. Nature *367*, 40–46.

Maugis, B., Brugués, J., Nassoy, P., Guillen, N., Sens, P., and Amblard, F. (2010). Dynamic instability of the intracellular pressure drives bleb-based motility. J. Cell Sci. *123*, 3884–3892.

Mim, C., and Unger, V.M. (2012). Membrane curvature and its generation by BAR proteins. Trends Biochem. Sci. *37*, 526–533.

Moreau, H.D., Piel, M., Voituriez, R., and Lennon-Duménil, A.-M. (2018). Integrating physical and molecular insights on immune cell migration. Trends Immunol. *39*, 632–643.

Mullins, R.D., Heuser, J.A., and Pollard, T.D. (1998). The interaction of Arp2/3 complex with actin: nucleation, high affinity pointed end capping, and formation of branching networks of filaments. Proc. Natl. Acad. Sci. USA *95*, 6181–6186.

Nguyen, T.T.T., Park, W.S., Park, B.O., Kim, C.Y., Oh, Y., Kim, J.M., Choi, H., Kyung, T., Kim, C.-H., Lee, G., et al. (2016). PLEKHG3 enhances polarized cell migration by activating actin filaments at the cell front. Proc. Natl. Acad. Sci. USA *113*, 10091–10096.

Paluch, E.K., and Raz, E. (2013). The role and regulation of blebs in cell migration. Curr. Opin. Cell Biol. *25*, 582–590.

Paluch, E.K., Aspalter, I.M., and Sixt, M. (2016). Focal Adhesion-Independent Cell Migration. Annu. Rev. Cell Dev. Biol. *32*, 469–490.

Pirrung, M.C., Drabik, S.J., Ahamed, J., and Ali, H. (2000). Caged chemotactic peptides. Bioconjug. Chem. *11*, 679–681.

Raucher, D., and Sheetz, M.P. (2000). Cell spreading and lamellipodial extension rate is regulated by membrane tension. J. Cell Biol. *148*, 127–136.

Saha, S., Nagy, T.L., and Weiner, O.D. (2018). Joining forces: crosstalk between biochemical signalling and physical forces orchestrates cellular polarity and dynamics. Philos. Trans. R. Soc. Lond. B, Biol. Sci. *373*.

Sanjana, N.E., Shalem, O., and Zhang, F. (2014). Improved vectors and genome-wide libraries for CRISPR screening. Nat. Methods *11*, 783–784.

Sasaki, A.T., Janetopoulos, C., Lee, S., Charest, P.G., Takeda, K., Sundheimer, L.W., Meili, R., Devreotes, P.N., and Firtel, R.A. (2007). G protein-independent Ras/PI3K/F-actin circuit regulates basic cell motility. J. Cell Biol. *178*, 185–191.

Sens, P., and Plastino, J. (2015). Membrane tension and cytoskeleton organization in cell motility. J Phys Condens Matter *27*, 273103.

Shakir, M.A., Jiang, K., Struckhoff, E.C., Demarco, R.S., Patel, F.B., Soto, M.C., and Lundquist, E.A. (2008). The Arp2/3 activators WAVE and WASP have distinct genetic interactions with Rac GTPases in Caenorhabditis elegans axon guidance. Genetics *179*, 1957–1971.

Soderling, S.H., Binns, K.L., Wayman, G.A., Davee, S.M., Ong, S.H., Pawson, T., and Scott, J.D. (2002). The WRP component of the WAVE-1 complex attenuates Rac-mediated signalling. Nat. Cell Biol. *4*, 970–975.

Srinivasan, S., Wang, F., Glavas, S., Ott, A., Hofmann, F., Aktories, K., Kalman, D., and Bourne, H.R. (2003). Rac and Cdc42 play distinct roles in regulating PI(3,4,5)P3 and polarity during neutrophil chemotaxis. J. Cell Biol. *160*, 375–385.

Stanley, A., Thompson, K., Hynes, A., Brakebusch, C., and Quondamatteo, F. (2014). NADPH oxidase complex-derived reactive oxygen species, the actin cytoskeleton, and Rho GTPases in cell migration. Antioxid. Redox Signal. *20*, 2026–2042.

Swaney, K.F., Huang, C.-H., and Devreotes, P.N. (2010). Eukaryotic chemotaxis: a network of signaling pathways controls motility, directional sensing, and polarity. Annu. Rev. Biophys. *39*, 265–289.

Ting-Beall, H.P., Needham, D., and Hochmuth, R.M. (1993). Volume and osmotic properties of human neutrophils. Blood *81*, 2774–2780.

Veltman, D.M., King, J.S., Machesky, L.M., and Insall, R.H. (2012). SCAR knockouts in Dictyostelium: WASP assumes SCAR's position and upstream regulators in pseudopods. J. Cell Biol. *198*, 501–508.

Wang, F., Herzmark, P., Weiner, O.D., Srinivasan, S., Servant, G., and Bourne, H.R. (2002). Lipid products of PI(3)Ks maintain persistent cell polarity and directed motility in neutrophils. Nat. Cell Biol. *4*, 513–518.

Weiner, O.D., Neilsen, P.O., Prestwich, G.D., Kirschner, M.W., Cantley, L.C., and Bourne, H.R. (2002). A PtdInsP(3)- and Rho GTPase-mediated positive feedback loop regulates neutrophil polarity. Nat. Cell Biol. *4*, 509–513.

Weiner, O.D., Rentel, M.C., Ott, A., Brown, G.E., Jedrychowski, M., Yaffe, M.B., Gygi, S.P., Cantley, L.C., Bourne, H.R., and Kirschner, M.W. (2006). Hem-1 complexes are essential for Rac activation, actin polymerization, and myosin regulation during neutrophil chemotaxis. PLoS Biol. *4*, e38.

Weiner, O.D., Marganski, W.A., Wu, L.F., Altschuler, S.J., and Kirschner, M.W. (2007). An actin-based wave generator organizes cell motility. PLoS Biol. *5*, e221.

Welch, M.D., Iwamatsu, A., and Mitchison, T.J. (1997). Actin polymerization is induced by Arp2/3 protein complex at the surface of Listeria monocytogenes. Nature *385*, 265–269.

Wilson, K., Lewalle, A., Fritzsche, M., Thorogate, R., Duke, T., and Charras, G. (2013). Mechanisms of leading edge protrusion in interstitial migration. Nat. Commun. *4*, 2896.

Xu, J., Wang, F., Van Keymeulen, A., Herzmark, P., Straight, A., Kelly, K., Takuwa, Y., Sugimoto, N., Mitchison, T., and Bourne, H.R. (2003). Divergent signals and cytoskeletal assemblies regulate self-organizing polarity in neutrophils. Cell *114*, 201–214.

Yang, H.W., Collins, S.R., and Meyer, T. (2016). Locally excitable Cdc42 signals steer cells during chemotaxis. Nat. Cell Biol. *18*, 191–201.

Yip, A.K., Chiam, K.-H., and Matsudaira, P. (2015). Traction stress analysis and modeling reveal that amoeboid migration in confined spaces is accompanied by expansive forces and requires the structural integrity of the membrane-cortex interactions. Integr Biol (Camb) *7*, 1196–1211.

SUPPLEMENTAL MATERIALS

Figure S1. Validation of CRISPR-mediated genome-editing via immunoblot.

Figure S2. Cellular actin levels and turnover in WAVE-null cells.

Figure S3. Computational simulations of membrane tension as a function of curvature of actin nucleators.

Videos 1-13.

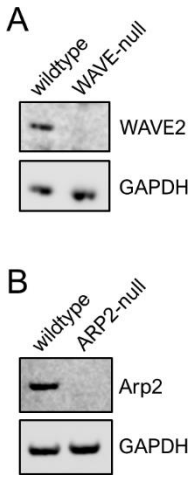

Figure S1. Validation of CRISPR-mediated genome-editing via immunoblot.

A) WAVE2 antibody immunoblots of wildtype and WAVE-null cells (i.e. lacking Hem-1, the hematopoietic-specific core component of WAVE complex). GAPDH was used as a loading control.

B) Arp2 antibody immunoblots of wildtype and WAVE-null cells. GAPDH was used as a loading control.

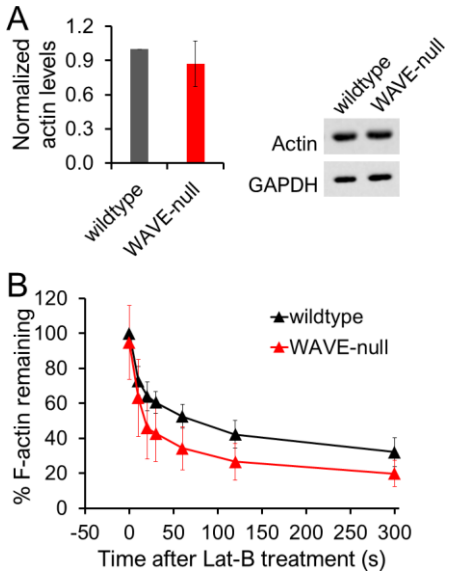

Figure S2. Cellular actin levels and turnover in WAVE-null cells.

A) Immunoblots of wildtype and WAVE-null cells using antibodies targeting actin. GAPDH was used as a loading control.

B) F-actin levels for cells at indicated timepoints post-treatment with 50 nM Latrunculin-B were determined by flow cytometry. Each point is an average of 4 independent experiments where the mean fluorescence of >10,000 cells was measured. P > 0.05 for wildtype and WAVE-null cells at every timepoint by unpaired t-test. Error bars, SD.

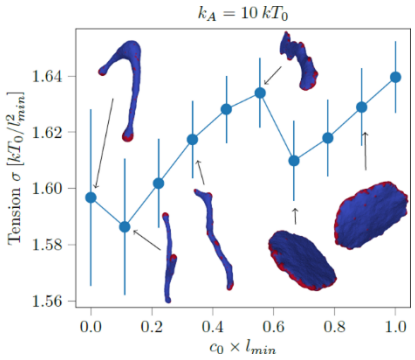

Figure S3. Computational simulations of membrane tension as a function of curvature of actin nucleators. Membrane tension σ (see "Materials and Methods") as a function of spontaneous curvature, c_0, of actin nucleators. Averaging was performed over 200 statistically independent microstates in equilibrium. Actin nucleators, red. Protein-free bilayer, blue. Error bars, SD. Note that the elastic constant of the membrane (K_A) is 10-fold larger than in simulations performed in **Fig. 2F**.

Video 1. Wildtype dHL-60s as in **Fig. 1C**, top panel imaged by DIC microscopy. Time, mm:ss.

Video 2. WAVE-null dHL-60s as in **Fig. 1C**, bottom panel imaged by DIC microscopy. Time, mm:ss.

Video 3. Wildtype dHL-60 expressing the Rac activity biosensor PakPBD-mCitrine imaged by confocal microscopy as in **Fig. 3B**, top panel. Each frame represents a single focal plane.

Video 4. WAVE-null dHL-60 expressing the Rac activity biosensor PakPBD-mCitrine imaged by confocal microscopy as in **Fig. 3B**, bottom panel. Each frame represents a single focal plane.

Video 5. Wildtype dHL-60 expressing the Rac activity biosensor PakPBD-mCitrine imaged by confocal microscopy as in **Fig. 5C**, top panel. Each frame represents a single focal plane.

Video 6. WAVE-null dHL-60 expressing the Rac activity biosensor PakPBD-mCitrine imaged by confocal microscopy as in **Fig. 5C**, bottom panel. Each frame represents a single focal plane.

Video 7. Wildtype dHL-60 expressing the Rac activity biosensor PakPBD-mCitrine imaged by confocal microscopy as in **Fig. 6B**, top panel. Each frame represents a single focal plane.

Video 8. Wildtype dHL-60s expressing the Rac activity biosensor PakPBD-mCitrine imaged by confocal microscopy as in **Fig. 6B**, bottom panel. Each frame represents a single focal plane.

Video 9. WAVE-null dHL-60 expressing the Rac activity biosensor PakPBD-mCitrine imaged by confocal microscopy as in **Fig. 6D**, top panel. Each frame represents a single focal plane.

Video 10. WAVE-null dHL-60 expressing the Rac activity biosensor PakPBD-mCitrine imaged by confocal microscopy as in **Fig. 6D**, bottom panel. Each frame represents a single focal plane.

Video 11. WAVE-null dHL-60s expressing the Rac activity biosensor PakPBD-mCitrine imaged by confocal microscopy. Cells were prepared as described in **Fig. 6A**. Confinement of cells was alternated between ‘weak’ (chamber height = 6.5 μm) and ‘strong’ (chamber height = 4.5 μm). Each frame represents a single focal plane.

Video 12. WAVE-null dHL-60s expressing the Rac activity biosensor PakPBD-mCitrine imaged by confocal microscopy. Cells were prepared as described in **Fig. 6A** and placed under ‘strong’ confinement. Each frame represents a single focal plane.

Video 13. WAVE-null dHL-60s expressing the Rac activity biosensor PakPBD-mCitrine imaged by confocal microscopy. Colored lines indicate cell boundaries (see “Materials and methods for details). Images were acquired at 1-s intervals.